

(SHERRY) JCMT-SCUBA2 High rEdshift bRight quasaR surveY - II: the environment of $z \sim 6$ quasars in sub-millimeter band

QIONG LI ^{1,2,3} RAN WANG ^{1,2} XIAOHUI FAN ⁴ XUE-BING WU ^{1,2} LINHUA JIANG ² EDUARDO BAÑADOS ⁵
BRAM VENEMANS ⁵ YALI SHAO ^{1,2} JIANAN LI ^{1,2} JEFF WAGG⁶ ROBERTO DECARLI ⁷ CHIARA MAZZUCHELLI ⁸
ALAIN OMONT ⁹ FRANK BERTOLDI ¹⁰ SEAN JOHNSON ¹¹ AND CHRISTOPHER J. CONSELICE ³

¹Department of Astronomy, School of Physics, Peking University, Beijing 100871, P. R. China

²Kavli Institute for Astronomy and Astrophysics, Peking University, Beijing, 100871, P. R. China

³Jodrell Bank Centre for Astrophysics, University of Manchester, Oxford Road, Manchester M13 9PL, UK

⁴University of Arizona (Steward Observatory), United States

⁵Max-Planck-Institut für Astronomie, Königstuhl 17, D-69117, Heidelberg, Germany

⁶Square Kilometre Array Observatory, Lower Withington, Macclesfield, Cheshire SK11 9FT, UK

⁷INAF – Osservatorio di Astrofisica e Scienza dello Spazio di Bologna, via Gobetti 93/3, I-40129, Bologna, Italy.

⁸European Southern Observatory, Alonso de Cordova 3107, Vitacura, Region Metropolitana, Chile

⁹Sorbonne Université, UPMC Université Paris 6 and CNRS, UMR 7095, Institut d’Astrophysique de Paris, France

¹⁰Universität Bonn (Argelander-Institut für Astronomie), Germany

¹¹Department of Astronomy, University of Michigan, 311 West Hall, 1085 S. University Ave, Ann Arbor, MI, 48109-1107, U.S.A.

(Received XXX; Revised XXX; Accepted XXX)

Submitted to ApJ

ABSTRACT

The formation of the first supermassive black holes is expected to have occurred in some most pronounced matter and galaxy overdensities in the early universe. We have conducted a sub-mm wavelength continuum survey of 54 $z \sim 6$ quasars using the Submillimeter Common-User Bolometre Array-2 (SCUBA2) on the James Clerk Maxwell Telescope (JCMT) to study the environments around $z \sim 6$ quasars. We identified 170 submillimeter galaxies (SMGs) with above 3.5σ detections at 450 or 850 μm maps. Their FIR luminosities are $2.2 - 6.4 \times 10^{12} L_{\odot}$, and star formation rates are $\sim 400 - 1200 M_{\odot} \text{ yr}^{-1}$. We also calculated the SMGs differential and cumulative number counts in a combined area of $\sim 620 \text{ arcmin}^2$. To a 4σ detection (at $\sim 5.5 \text{ mJy}$), SMGs overdensity is $0.68_{-0.19}^{+0.21} (\pm 0.19)$, exceeding the blank field source counts by a factor of 1.68. We find that 13/54 quasars show overdensities (at $\sim 5.5 \text{ mJy}$) of $\delta_{SMG} \sim 1.5 - 5.4$. The combined area of these 13 quasars exceeds the blank field counts with the overdensity to 5.5 mJy of $\delta_{SMG} \sim 2.46_{-0.55}^{+0.64} (\pm 0.25)$ in the regions of $\sim 150 \text{ arcmin}^2$. However, the excess is insignificant on the bright end (e.g., 7.5 mJy). We also compare results with previous environmental studies of Lyman alpha emitters (LAEs) and Lyman-Break Galaxies (LBGs) on a similar scale. Our survey presents the first systematic study of the environment of quasars at $z \sim 6$. The newly discovered SMGs provide essential candidates for follow-up spectroscopic observations to test whether they reside in the same large-scale structures as the quasars and search for protoclusters at an early epoch.

Keywords: Quasars (1319), Submillimeter astronomy (1647), Active galaxies (17)

1. INTRODUCTION

More than 200 quasars at $z > 5.6$ were discovered in optical and near-infrared surveys, such as SDSS (e.g. Jiang et al. 2008; Fan et al. 2006), CFHQS (e.g. Willott et al. 2007; Willott et al. 2010), UKIDSS (e.g. Venemans et al. 2007; Mortlock et al. 2011), VIKING (e.g.

Venemans et al. 2013; Venemans et al. 2015), VST-ATLAS (Carnall et al. 2015), DES (Reed et al. 2015; Yang et al. 2019), HSC (Matsuoka et al. 2016), Pan-STARRS1 (e.g. PS1; Bañados et al. 2014; Bañados et al. 2016; Wang et al. 2019), etc (e.g. Yang et al. 2021). Galaxy formation simulations and cosmological models predict that high redshift quasars reside in the most massive dark matter halos and grow quickly in the galaxy overdensity environments formed by the hierarchical merging of galaxies (e.g. Romano-Díaz et al. 2011; Costa et al. 2014). Discovering the overdensities of galaxies associated with $z \sim 6$ quasars will trace mass assembly and probe the evolution of protoclusters and large-scale structures in the early universe. Hence, it is a chance to investigate the environment where QSOs hosting SMBHs reside and to search for galaxy protoclusters close to the end of cosmic reionization.

Over the last twenty years, sub-mm surveys around AGNs and galaxies have advanced our understanding of the galaxy environment at the cosmic time. The first one was uncovered by SCUBA (Submillimeter Common-User Bolometre Array) surveys on JCMT (the James Clerk Maxwell Telescope, Smail et al. 1997). Subsequently, a series of papers have shown evidence for overdensities of submillimeter galaxies (SMGs) at $z = 2 \sim 3$ in the vicinities of luminous radio galaxies (e.g., De Breuck et al. 2004; Greve et al. 2007) and dust absorbed QSOs (Stevens et al. 2004; Priddey et al. 2007). The clustering of SMGs at $z \sim 2$ around luminous QSOs or galaxies indicates evolutionary scenarios in which powerful starbursts and QSOs occur in the same systems (Hickox et al. 2012). And Priddey et al. (2008) also reported deep sub-mm images with a large field of view for three $z > 5$ quasars in SCUBA observations. However, the observational evidence of large-scale structure close to $z \sim 6$ quasars is elusive, limited by a relatively small quasar sample size and strong selection biases of quasars.

There are many different approaches for tracing overdense regions around quasars or galaxies at $z \sim 6$, such as Lyman-Break Galaxies (LBGs) selected via broadband optical/NIR colors (Stiavelli et al. 2005; Morselli et al. 2014) or Lyman alpha emitters (LAEs) selected via narrow/broadband observations (e.g., Mazzucchelli et al. 2017; Ota et al. 2018). Despite the huge investment of optical or near-infrared (NIR) telescope time, the galaxy environments surrounding $z \sim 6$ quasars remain unconstrained. Overdensities of galaxies were discovered with deep optical imaging around several quasars at $4 < z < 6$ (e.g., the $z = 6.28$ quasar SDSS J1030+0524 in Stiavelli et al. 2005, and the $z = 5.81$ radio-loud quasar SDSS J0836+0054 in Zheng et al. 2006 and Ajiki

et al. 2006). However, some works failed to find any significant galaxy overdensity (e.g., LAEs surrounding PSO J215-16 at $z = 5.73$ in Mazzucchelli et al. 2017, and CFHQS J2329-0301 in Goto et al. 2017). Integral field spectroscopic investigations at radio/sub-mm wavelengths in quasar fields both with ALMA (Decarli et al. 2017; Willott et al. 2017; Venemans et al. 2019) and NOEMA (Wang et al. 2011; Omont et al. 2013) revealed the presence of close (< 50 kpc, < 1 cMpc) companion galaxies in the immediate proximity of the first massive black holes. It only traces the small-scale clustering at close separation from the central quasars.

To test whether the companion galaxies identified around some $z \sim 6$ quasars are a small-scale phenomenon or the expression of the long-sought large-scale overdensities postulated by the models, in 2016-2018 we mapped the fields around 54 quasars at $z \sim 6$ over a much larger field-of-view ($\sim 15'$ in diameter) using SCUBA-2 (Submillimeter Common-User Bolometre Array-2) on JCMT, named as ‘JCMT-SCUBA2 High rEdshift bRight quasaR surveY’ (‘SHERRY’ survey). SCUBA-2 has a field of view of 64 sq-arcminutes (only 4.3 sq-arcmins for SCUBA) - a factor of 16 times improvement over SCUBA (Chapin et al. 2013). And it has the fastest mapping speed at 450 μm and 850 μm , which makes searching for SMGs more efficient (Chapin et al. 2013). The SHERRY survey is the first to build a large, statistical sample of $z \sim 6$ quasars for sub-mm observation, including $\sim 20\%$ of the $z \sim 6$ quasars discovered to date.

In the first paper of this survey (SHERRY-I, Li et al. 2020a), we reported that about 30% (16/54) quasars were detected with a typical 850 μm RMS sensitivity of 1.2 mJy beam $^{-1}$ ($> 3.5\sigma$). The broadband SED for $z \sim 6$ quasars is similar to that at $z \sim 2$, which indicates there is probably no evolution of quasars’ properties with redshift. The optical/near-infrared (NIR) spectra of these objects show 11% (6/54) of the sources have weak ultraviolet (UV) emission line features. The SHERRY survey also indicates that quasars with sub-mm detections tend to have weaker emission lines than quasars with non-detections. The weak-line quasar at $z \sim 6$ may be a young AGN-galaxy system (Li et al. 2020a), in which the broad line region is starting to develop slowly and have some unusual properties.

In this paper, we present JCMT/SCUBA-2 observations of the environment around the quasars at $5.6 < z < 7.1$ and search for galaxy protoclusters close to the end of cosmic reionization. We describe the SCUBA2 observations and data reduction in Section 2. In Section 3, we introduce our method to extract SMGs candidates and calculate the number counts. We present the num-

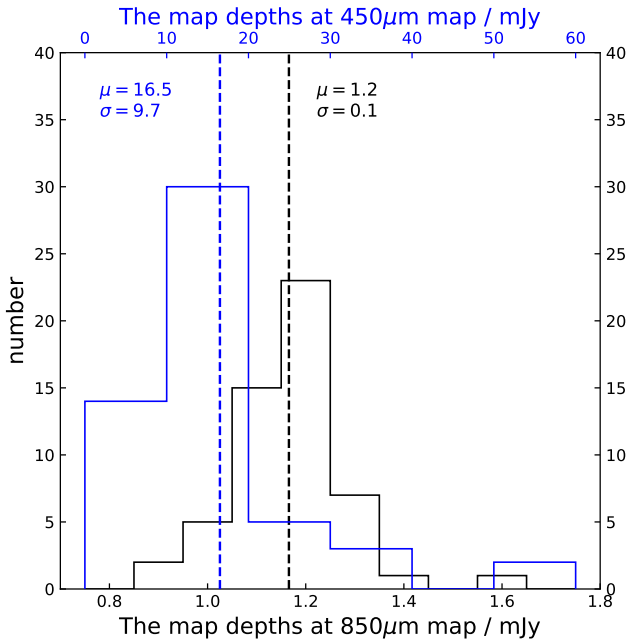


Figure 1. The distribution of the map depth at 850 and 450 μm .

ber counts results and the discussions in Section 4. Finally, we give a summary of the main results in Section 5. We adopt a Λ -model cosmology with $H_0 = 71 \text{ km s}^{-1} \text{ Mpc}^{-1}$, $\Omega_M = 0.27$ and $\Omega_\Lambda = 0.73$ (Spergel et al. 2007) throughout this paper.

2. SCUBA2 OBSERVATIONS AND DATA REDUCTION

We observed 54 quasars at $5.7 < z < 7.1$, which have rest-frame 1450 \AA absolute magnitudes of $M_{1450} \leq -25.4$. The observations were carried out with the SCUBA2 camera on the JCMT in Hawaii from August 2015 to January 2018 (Program ID: M15BI055, M16AP013, M17AP062, M17BP034). We used ‘the constant velocity Daisy scan’ observation mode (‘CV DAISY’ mode) with the field of view of $15'$ in diameter. This mode is for small and compact sources of order 3-arcmin or less. The most uniform and best rms region is the central one with a diameter of about $4'$, corresponding to comoving $9.8 \text{ h}^{-1} \text{ Mpc}$ comoving. This covers typical protocluster scales at $z \sim 6$ (e.g., Overzier et al. 2009).

SCUBA2 observes two bands, 450 μm and 850 μm simultaneously. The main beam sizes of SCUBA-2 are $7.9''$ at 450 μm and $14.9''$ at 850 μm ; with the spatial resolution of $4''$ / pixel and $2''$ / pixel, respectively. The observations were carried out in grade 2 / grade 3 weather conditions with precipitable water vapor (PWV) of 0.83 - 2.58 mm at zenith (atmospheric

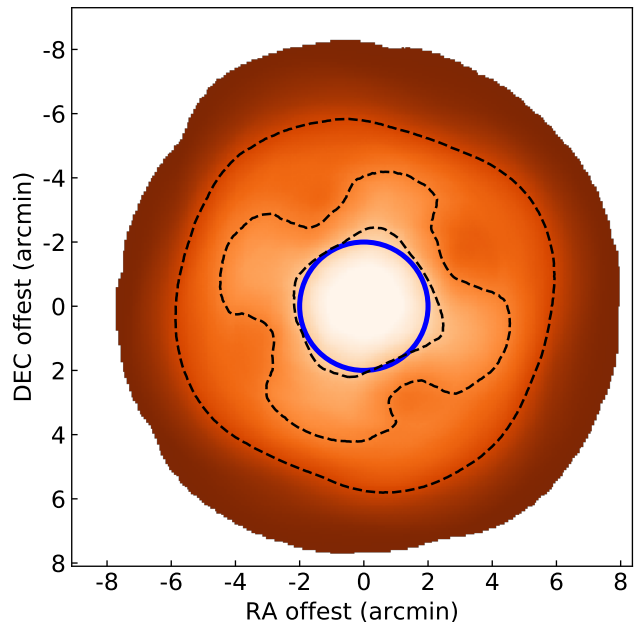


Figure 2. Example SCUBA2 exposure time map. The contours denote the 20, 40, 60% exposure time levels compared to the maximum level on the map. The blue circle region has a diameter of $4'$ and marks the region with uniform and low RMS for SMG overdensity searches.

optical depth $0.05 < \tau_{225\text{GHz}} < 0.12$). We observed each target in four to six ~ 30 -minute scans with a total on-source time of 2–3 hours to reach the sensitivity of 1.2 mJy at $850 \mu\text{m}$. We present the details of the observations in Li et al. (2020a). The calibrated sources were observed before and after the target sources and selected from the James Clerk Maxwell Telescope (JCMT) calibrator list (Dempsey et al. 2013). Calibration sources included Mars, Uranus, Neptune, etc.

We reduced the data using the STARLINK SCUBA-2 science pipeline with the configuration file of ‘dim-config blank field.lis’, which is the recipe for processing maps containing the faint compact sources (Chapin et al. 2013). We processed each complete observation separately to produce an image and calibrated it with the flux conversion factors (FCFs) to mJy/beam . We adopted the default FCFs value of $537 \pm 24 \text{ Jy pW}^{-1} \text{ beam}^{-1}$ for 850 μm map and $491 \pm 67 \text{ Jy pW}^{-1} \text{ beam}^{-1}$ for 450 μm map (Dempsey et al. 2013). We combined all images for a given source into a single image using inverse-variance weighting. Using this recipe, we further processed the output map with a beam-match filtered of a $15''$ FWHM Gaussian at 850 μm band. The S/N is taken to enhance point sources, which is suitable for searching for SMGs at $z \sim 6$. The final 850- and 450- μm maps have typical noise levels of 1.2 and 16.5 mJy beam^{-1} , shown in Figure 1.

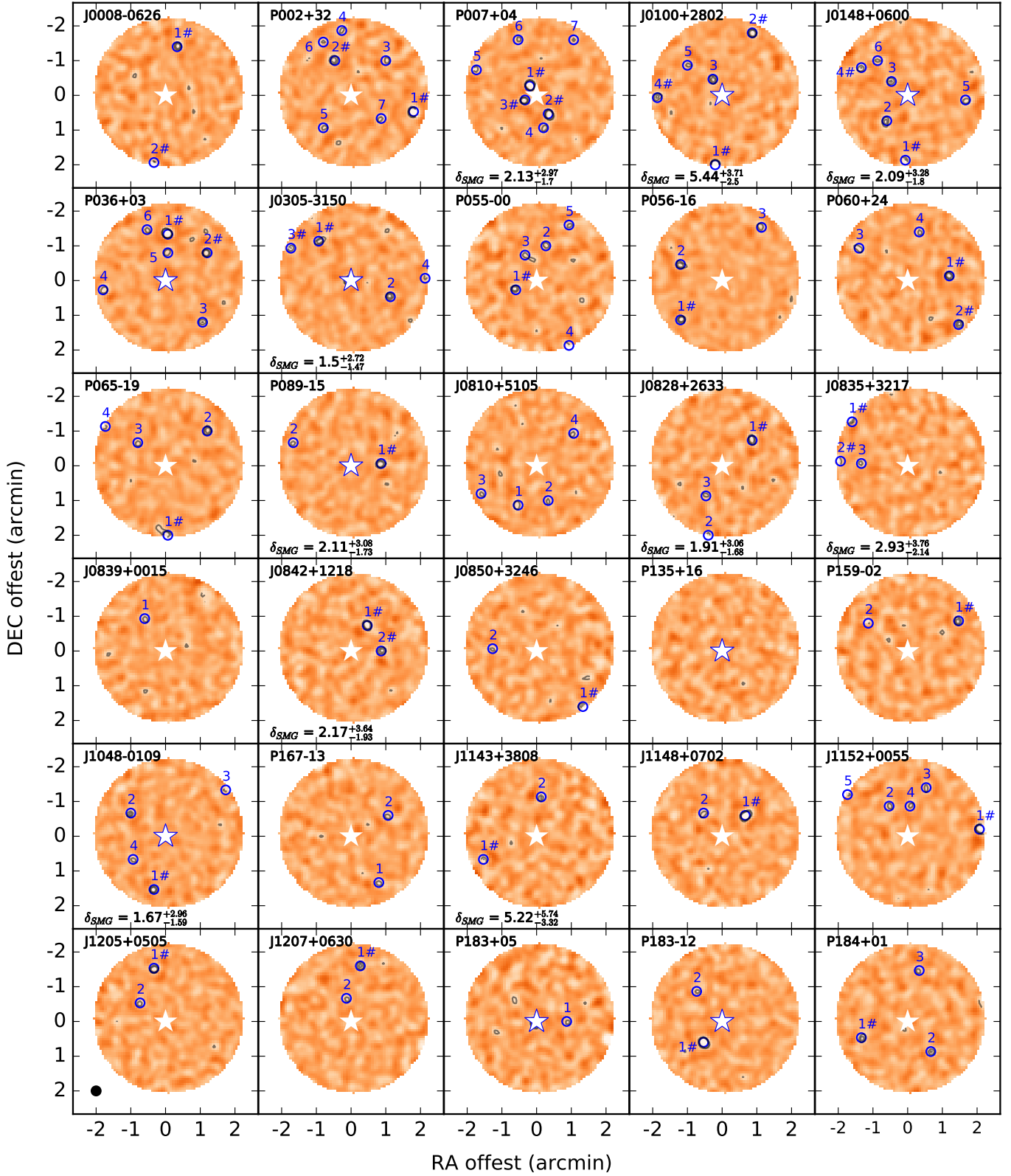


Figure 3. JCMT-SCUBA2 850 μ m images of the surrounding regions around 54 $z \sim 6$ quasar with a beam size of FWHM = 15". The selected region is within 2.23 arcmins from the quasar optical position (which covers typical protocluster scales at $z \sim 6$) and has one sigma uncertainty of < 1.5 mJy beam $^{-1}$ for each pixel. The contour levels are +3, +4, +5, +6, +7 \times 1.5 mJy beam $^{-1}$ for each map. The star indicates the quasar optical/NIR position. The star with the blue edge is the sub-mm detected quasars. The blue circles indicate the selected SMGs (with S/N $>$ 3.5 at 850um or 450um, see Table 2). The sources marked with '#' are the SMGs used in the overdensity analysis with deboosted fluxes $>$ 5.5 mJy.

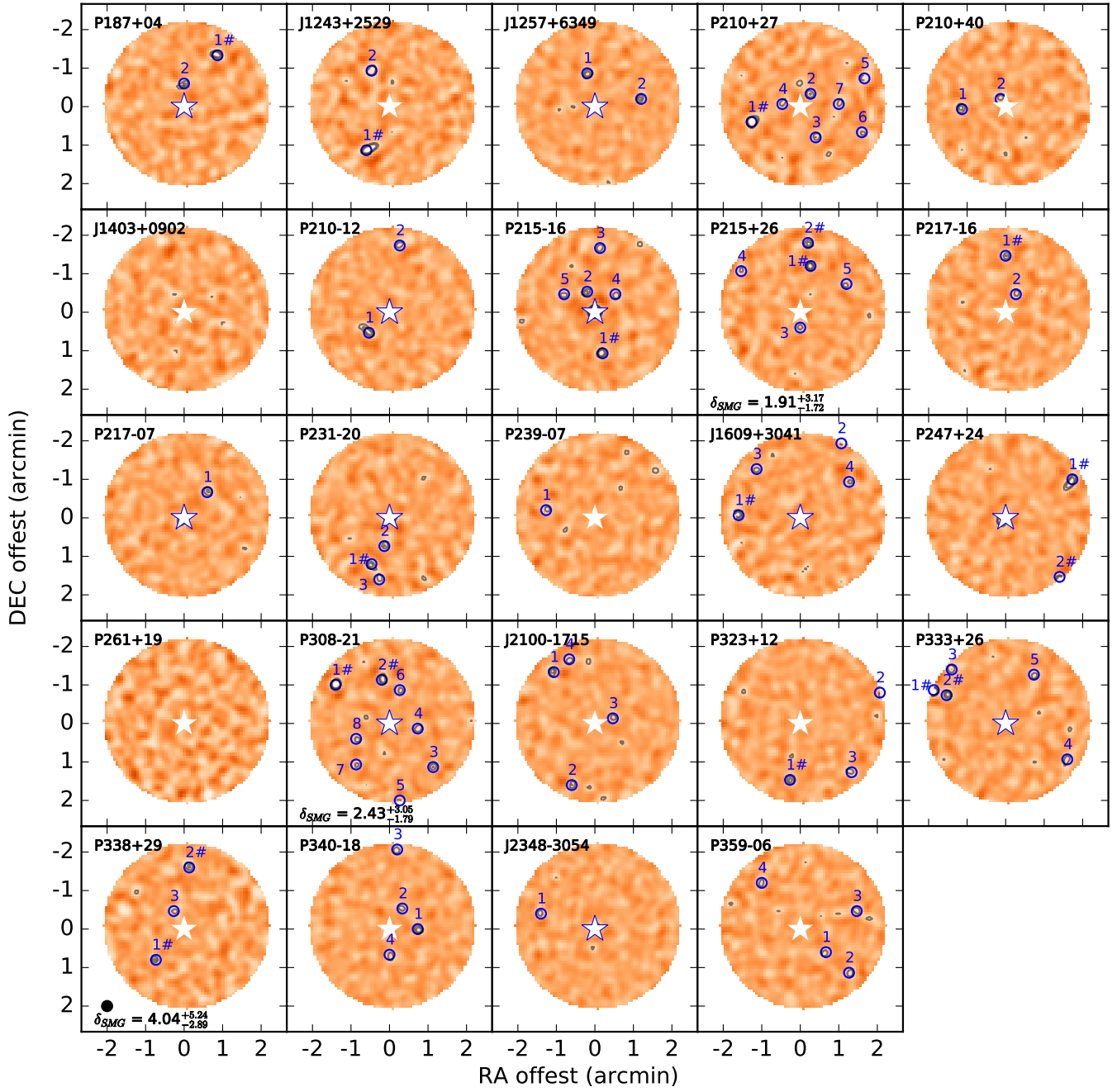


Figure 4. -Continued

3. SOURCE EXTRACTION AND NUMBER COUNTS

3.1. Source extraction

The SHERRY survey fields are centered on the targeted $z \sim 6$ quasars. The expected protocluster size is about ~ 20 cMpc along the side, and the core of the protocluster is 2 - 3 cMpc (Overzier et al. 2009; Chiang et al. 2017). For each map, we use the (square root of the) exposure time as a proxy for noise, which is as a function of radius (Figure 2). Note the actual noise map is produced from the pipeline, including other noise, e.g., the instrument and atmospheric noise. Considering that the noise increases rapidly at a large radius of the Daisy maps, we searched for overdensity within the central ~ 2 arcmins around the quasar. This region corresponds to a scale of ~ 10 cMpc in diameter, which can trace a typical protocluster (Chiang et al. 2013). Furthermore, we mask the region where the RMS noise level is > 1.5 mJy beam $^{-1}$ based on the error map to ensure the best/uniform sensitivity in the SCUBA-2 images. The error difference between the center and the edge is less than $\sim 15\%$. The source extraction is processed in this effective region, shown in Figure 3.

To extract the sources in the maps, we adopted the ‘top-down’ algorithm to find the source with the highest SNR in the two bands maps for each quasar field (e.g., Chen et al. 2013; Geach et al. 2017). SMGs at high redshifts are unresolved in SCUBA-2 observations; thus, the flux density of the source is the peak value of the pixels in the beam. We first identified the pixel’s position with the highest SNR for each source. Then we subtracted a scaled point spread function (PSF) from the image at the source position. We generated the Gaussian PSF model with an FWHM of 14.9 arcsec at $850 \mu\text{m}$ map and 7.9 arcsec at $450 \mu\text{m}$. During each iteration, we recorded the coordinates, flux densities, noise values, and SNRs of each $> 3.0\sigma$ detection of candidate sources. To create a unique source list, we removed multiple detections if the secondary peaks were within one beam area of a higher SNR one. We iterated this process until there were no more sources with SNR of greater significance than the threshold in the image.

After identifying the $> 3.0\sigma$ candidate sources in the two band maps, we cross-checked the sources between $850\mu\text{m}$ and $450\mu\text{m}$ maps to find the counterpart in the radius of $15''$ (the beam size at $850\mu\text{m}$ map). The final catalog of submm source candidates is generated as those satisfying $> 3.5\sigma$ at least in one band. The flux density of its counterpart on another band is also listed in the catalog, if it has. The $850\mu\text{m}$ images of each of the 54 quasar fields are shown in Figure 3. The final

SMGs selected as described above are marked as blue circles, and listed in Table 2 of Appendix A. We also carried out MCMC deboosted process for each individual source’s flux for repeating 50000 times, and calculated the deboosted flux and its error.

3.2. Number counts

In this section, we determine the pure galaxy number counts in the quasar fields. To do so, we first need to estimate the number of spurious sources contaminating the counts and estimate completeness levels, particularly at low SNR. These completeness and flux deboosting calculations are all processed for each field individually. In this section, we use SDSS J0100+2802 as an example to show how it works. Note the number counts result in this paper is only based on $850 \mu\text{m}$ maps due to its better sensitivity.

3.2.1. Spurious source

We examined the negative noise statistics to calculate the contamination rate of false detections. For example, we plot the S/N histograms of the pixels in the effective area of the signal maps at quasar nearby field for SDSS J0100+2802 ($z = 6.3258 \pm 0.0010$) in $850\mu\text{m}$ and $450\mu\text{m}$ bands, in Figure 5. The red line represents the Gaussian fitting of the noise statistics. The excess above this line on the positive side represents true detections assuming that the noise is symmetric. On the other hand, the negative tail is from the spurious sources due to the matched-filter PSF (Chapin et al. 2013). We need to estimate the distribution of negative to obtain the pure number counts.

We performed this check on each field individually. We first constructed an inverted flux map and then applied the source extraction procedure described in Section 3.1 to them. Nine detections at $\sigma > 4$ were found in the inverted maps at $850\mu\text{m}$ band. We estimated the false detection rate above 4σ significance to be 11.4% (9/79). We also estimated the false detection rate at $3 < \sigma < 4$ to be 57.6% (57/99). Considering the effects of spurious sources, we calculate the number counts with the flux bin beginning from 4σ . Then the impact of the spurious source will significantly diminish, and the conclusions below are not affected.

3.2.2. Completeness

To describe how we make some corrections to calculate the number counts, we still use the field of quasar SDSS J0100+2802 ($z = 6.3258 \pm 0.0010$) as an example in the following. The completeness is the rate at which a source is expected to be detected in the image (Hatsukade et al. 2016). We used the Monte Carlo simulation approach to estimate completeness. The completeness

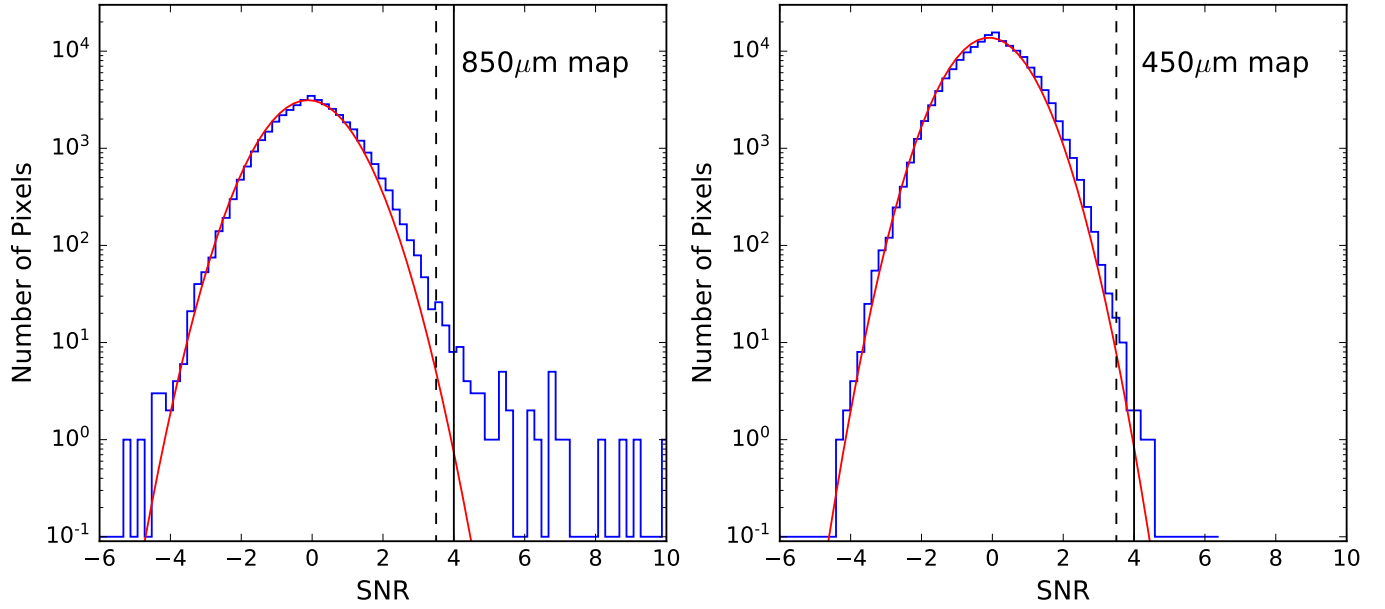


Figure 5. The S/N histograms of the signal maps in the field of quasar SDSS J0100+2802 ($z = 6.3258 \pm 0.0010$) in the $850\mu\text{m}$ and $450\mu\text{m}$ bands. The dashed and solid lines indicate the 3.5σ and 4σ . The red line represents the Gaussian fitting of the noise statistics.

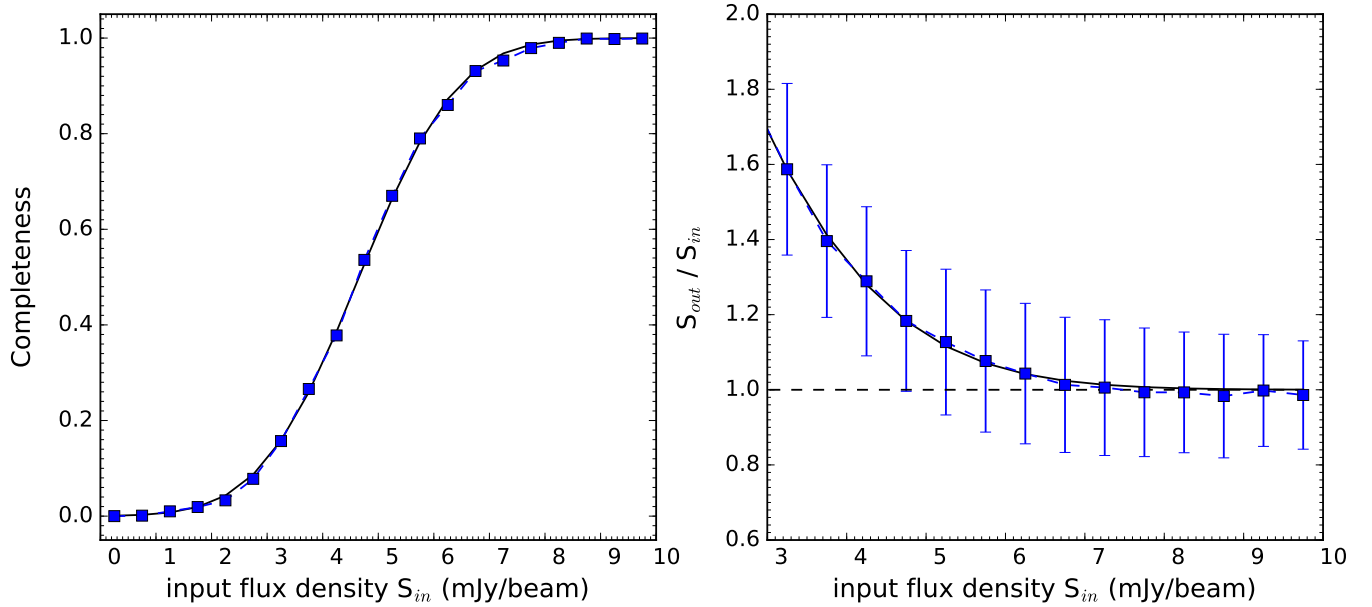


Figure 6. Example completeness and flux boosting estimates based on Monte Carlo source insertion. Left: Completeness as a function of input flux (S_{in}). The solid curve represents the best-fit function of $f(S_{in}) = [1 + \text{erf}((S_{in} - A)/B)]/2$ with best fitting parameters give in the text. Right: The ratio between input flux density and output flux density as a function of input flux. Error bars show 1σ of 5000 trials. Solid curve represents the best-fit function of $f(S_{in}) = 1 + A \exp(-BS_{in}^C)$. (Hatsukade et al. 2016).

test is only in the central best/uniform-sensitivity regions. We injected artificial sources of 0 – 10 mJy/beam at random positions in the maps $> 8.0''$ away from $\geq 3\sigma$ peaks to avoid the contribution from nearby sources. The flux bin step is 0.5 mJy for 850 μm map. Then we ran the source extraction on the maps to see if we could recover the injected sources. When the output source is above 3σ , the source is considered to be recovered. This procedure is repeated 5000 times for each flux bin. We fit the completeness as a function of $f(S_{in}) = [1 + \text{erf}((S_{in} - A)/B)]/2$ (Hatsukade et al. 2016), as shown in Figure 6. Here S_{in} is the input flux density. The best-fitted parameters are $A = 4.67 \pm 0.01$, $B = 2.05 \pm 0.02$. Based on this Monte-Carlo experiment, we estimate a 50% completeness level for 4.7 mJy point sources and 80% for 5.9 mJy point sources in 850 μm map.

3.2.3. flux boosting

With the Monte Carlo simulations, we also considered the effect that flux densities of low S/N sources are boosted (Murdoch et al. 1973; Hatsukade et al. 2016). More specifically, we calculated the ratio between the flux of the recovered sources and those of the injected artificial sources. We then estimate the mean ratio in 0.5 mJy flux bins. To illustrate this process, we plot the mean flux boosting value for the field of J0100 in Figure 6 (right). The flux boosting is more pronounced for low S/N sources. We fit the ratio between input flux density and output flux density as a function of $f(S_{in}) = 1 + A \exp(-BS_{in}^C)$ (Hatsukade et al. 2016). The best fitted parameters are $A = 1.74 \pm 0.27$, $B = 0.11 \pm 0.04$ and $C = 1.95 \pm 0.22$. At S/N = 4 (input flux = 4.8 mJy), the estimated mean flux boosting factor is 1.19 at 850 μm map. This is consistent with the results of Monte Carlo simulations in previous SCUBA studies (Eales et al. 2000; Scott et al. 2002; Cowie et al. 2002; Casey et al. 2013; Chen et al. 2013), such as the boosting factor of 1.25 at 850 μm map in Cowie et al. (2002). Potential contamination for the SMG number counts is the gravitational lensing effects of foreground objects (e.g., Chen et al. 2011). If some of the detected submillimeter sources are lensed background sources, they may increase the uncertainties of the source positions and also boost the measured fluxes. (Knudsen et al. 2008)

4. RESULTS AND DISCUSSION

4.1. Differential and cumulative number counts

To obtain an unbiased estimate of the number counts for each SMG candidate, we statistically correct the observed flux density using the Monte Carlo simulation for

each field, see Figure 6. Then, the deboosted flux density is amended for completeness, as described in Section 3.2.2. Note we also removed the quasar itself in the analysis of number counts.

There are two number counts to describe the source abundance: the cumulative number counts and the differential number counts. To study the general environment of $z \sim 6$ quasars, we built a combined area to calculate the differential number counts, which have independent errors for each count measurement, making it straightforward to do fitting. The combined area includes all 54 quasar nearby fields and totals ~ 620 arcmin², corresponding to ~ 3700 cMpc² (~ 76 pMpc²) at $z \sim 6$. It represents the overall environmental property of quasar fields at $z \sim 6$. Another number count is the cumulative number count. It applies to the small sample size with a visual underlying counts shape. This method can be used in the analysis of individual quasar nearby fields.

The differential number counts of the combined area are calculated by dividing each $> 3.5\sigma$ detection by the total combined area and adding up all measurements lying with each flux bin, then dividing by the flux width. Following previous studies, we fit the differential number counts with a Schechter function of the form (Casey et al. 2013; Geach et al. 2017):

$$\frac{dN}{dS} = \left(\frac{N_0}{S_0}\right) \left(\frac{S}{S_0}\right)^\alpha \exp\left(-\frac{S}{S_0}\right) \quad (1)$$

We find the best fit parameters are $N_0 \sim 3000 \text{deg}^{-2}$, $S_0 \sim 1.2$ mJy and $\alpha \sim 1.5$. We show the corrected differential and cumulative number counts for the effective area of the 54 quasars, together with the fit results in Figure 7. We list the corrected data points in Table 1. Note that our fitting is restricted to sources brighter than 5.5 mJy. The first set of uncertainties is Poisson errors (Gehrels 1986). And the second reflects the field variance that we used a bootstrapping approach. The individual field was selected randomly as many times as the size of a given sample, allowing for replacements, to create a new sample to calculate the counts. And each source is also corrected deboosting and completeness. This process was repeated 1000 times, and then we fitted a normal distribution to these 1000 realizations. The standard deviation of this distribution was the field variance. These variances are of comparable magnitude to the Poisson errors.

We then compared our results with the previous blank field survey - SCUBA2 Cosmology Legacy Survey (S2CLS, $\sim 5 \text{ deg}^2$) at 850 μm . To a 4σ detection (~ 5.5 mJy), the SMGs overdensity ($\delta_{\text{SMG}} = \rho_{\text{SMG}} / \rho_{\text{SMG}} < -1$) is $0.68^{+0.21}_{-0.19} (\pm 0.19)$ in the combined field

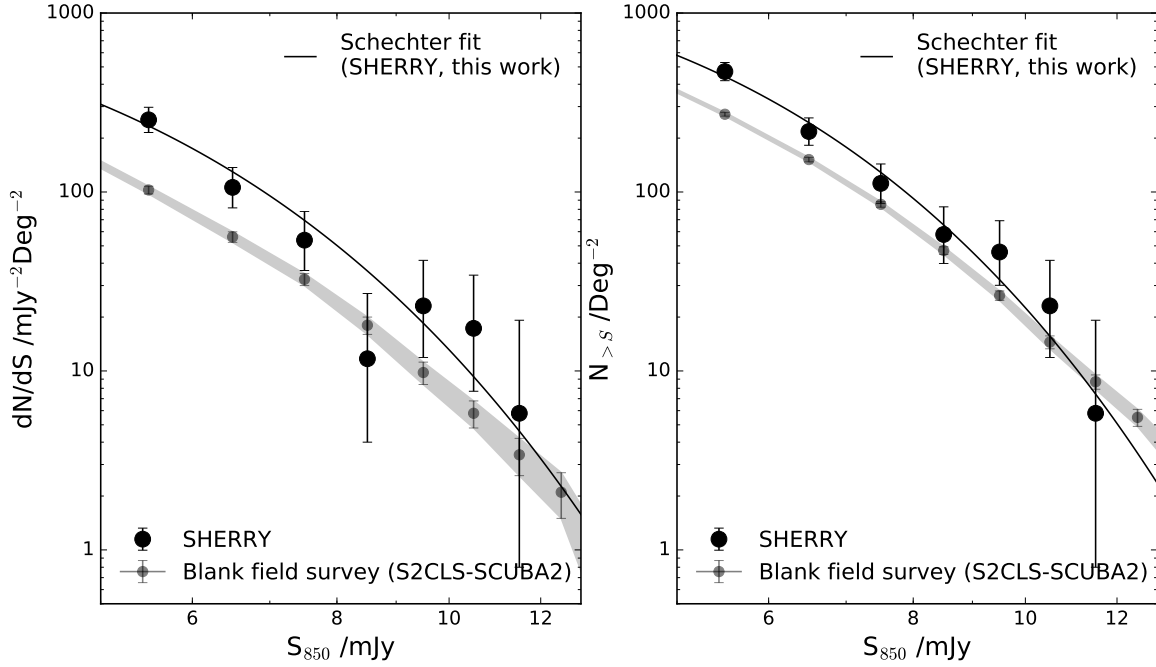


Figure 7. The combined differential and cumulative number counts at $850\mu\text{m}$ from all of our source fields. The filled black points and black lines indicate our data and Schechter fitting, respectively. The gray line shows the blank-field number counts of SMGs in the S2CLS field in Geach et al. (2017). For clarity, we only show the error bars of S2CLS and our data from Poissonian statistics (Gehrels 1986). Points in this work have been corrected for flux boosting and incompleteness (see figure 6).

Table 1. The combined differential and cumulative number counts at $850\mu\text{m}$

S_{860} (mJy)	dN	dN_{corr}	dN/dS ($\text{mJy}^{-1}\text{deg}^{-2}$)	$N(>S)$ (deg^{-2})
5.5	29	$42.2^{+7.6}_{-6.5}(\pm 7.4)$	$243.5^{+43.6}_{-37.4}(\pm 40.1)$	$461.4^{+57.6}_{-51.5}(\pm 53.4)$
6.5	16	$18.4^{+5.4}_{-4.3}(\pm 4.5)$	$106.1^{+31.0}_{-24.6}(\pm 24.9)$	$217.9^{+41.6}_{-35.4}(\pm 33.9)$
7.5	9	$9.3^{+4.2}_{-3.0}(\pm 2.6)$	$53.9^{+24.1}_{-17.4}(\pm 15.4)$	$111.8^{+31.7}_{-25.2}(\pm 22.1)$
8.5	2	$2.0^{+2.7}_{-1.3}(\pm 1.4)$	$11.7^{+15.4}_{-7.7}(\pm 8.3)$	$57.9^{+24.7}_{-18.1}(\pm 16.4)$
9.5	4	$4.0^{+3.2}_{-1.9}(\pm 1.9)$	$23.1^{+18.4}_{-11.2}(\pm 11.2)$	$46.2^{+22.9}_{-16.1}(\pm 14.3)$
10.5	3	$3.0^{+2.9}_{-1.7}(\pm 1.7)$	$17.3^{+17.0}_{-9.6}(\pm 9.6)$	$23.1^{+18.4}_{-11.2}(\pm 11.5)$
11.5	1	$1.0^{+2.3}_{-0.9}(\pm 1.0)$	$5.8^{+13.4}_{-5.0}(\pm 5.8)$	$5.8^{+13.4}_{-5.0}(\pm 5.8)$

NOTE—

S is the bin central flux density, and the bin width is one mJy. The first set of uncertainties is Poissonian errors. And the second reflects a bootstrap analysis error that is the standard deviation of counts in each bin after 1000 realizations of the random sampling. These uncertainties are of comparable magnitude to the Poisson errors. The combined area includes all 54 quasar nearby fields as a statistical field with the size of $\sim 620 \text{ arcmin}^2$, corresponding to $\sim 3700 \text{ cMpc}^2$ ($\sim 76 \text{ pMpc}^2$) at $z \sim 6$.

of 0.17 degree², exceeding ($\sim 1.68 \times$) the source counts of blank sky area. And to a 5σ detection, the SMG overdensity is a factor of $0.40_{-0.23}^{+0.27}(\pm 0.24)$. If the galaxy excess is mainly due to overdensities at a narrow redshift range around $z \sim 6$, the SMG overdensity near quasar redshifts must be higher.

To investigate which quasars reside in an overdense environment and search for protoclusters at $z \sim 6$, we also calculated the completeness and boosting corrected SMG cumulative number counts $N(>S)$ individually for each quasar field. We compared the results with the number counts in the blank field and gave a rough definition of ‘overdensity’. The lower limit of the SMGs cumulative number counts to 5.5 mJy ($\sim 4\sigma$) is above the value in the blank field. With this criterion, 13 quasar fields show clear sub-mm overdensities with the overdensity of $\delta_{SMG} \sim 1.5 - 5.4$. We label their overdensity in Figure 3. Here the calculation of the overdensity is based on the sources with deboosted fluxes brighter than 5.5 mJy. There are 55 sources from the whole survey (marked with ‘#’ in Figure 3). 24 of these lie in the 13 over-densities fields, with four of the over-densities comprise just one source above this flux limit.

We also combined the overdense fields around these 13 quasars and compared them with the blank field and those around other lower redshift galaxies. For comparison we show the cumulative number counts of SMGs, in fields centered on (i) luminous high-redshift AGN: $z \sim 5$ optically selected quasars (Priddey et al. 2008); $z \sim 4$ radio galaxies (Stevens et al. 2003); (ii) $z \sim 2$ protoclusters (Zhang et al. 2022); (iii) $z \sim 1$ clusters (Best 2002; Webb et al. 2005) and (iv) $z \sim 6$ optically selected quasars (in this paper) in Figure 8. The black line shows the blank field number counts of SMGs from the SCUBA2 survey of the S2CLS field in Geach et al. (2017). The combined field of these 13 quasars exceeds the blank field counts with the overdensity to 5.5 mJy of $\delta_{SMG} \sim 2.46_{-0.55}^{+0.64}(\pm 0.25)$ in the regions of ~ 150 arcmin². It is consistent with the lower redshift cluster and the surrounding regions of quasars and radio galaxies. But to the bright end, the excess is not significant, e.g., to 7.5 mJy, the overdensity decreases to $1.00_{-0.74}^{+1.08}(\pm 0.73)$. Compared with the lower redshift galaxies/quasar fields or cluster fields, the combined overdense area shows a lower overdensity. That is because the data from the literature are case studies that intentionally target overdense regions (including significant selected bias). Still, our data points represent the average environmental properties around $z \sim 6$ quasars, and overdensity is diluted.

Therefore, considering the abundant SMGs candidates in the faint-end, we select the fields where the lower limit

of the SMGs cumulative number counts to 6.5 mJy ($\sim 5\sigma$) is above the value in the blank field. There are three (3/13) $z \sim 6$ fields that show a significant excess over the blank field: P007+04 ($z = 6.0$), J0100+2801 ($z = 6.3$) and P308-21 ($z = 6.2$), shown in Figure 8. They are more likely similar to the lower redshift overdense fields/clusters with the overdensity of 2.1 - 5.4 at 5.5 mJy. However, Champagne et al. 2018 analyzed 1.2 mm ALMA dust continuum maps for 35 bright quasars at $z \sim 6$. They reported there is no evidence of 0.1 - 1mJy millimeter continuum sources in the environments of P007+04 ($z = 6.0$) and P308-21 ($z = 6.2$). The overdensity is -0.07 ± 0.56 , which implies no detected overdensity of dusty galaxies around these quasars. This conclusion is based on a small ALMA field of view of about $25''$, corresponding to an angular diameter distance of ~ 1 cMpc at $z \sim 6$. It could miss the overdensity on scales larger than one cMpc.

4.2. Correlation with LAE and LBG at $z \sim 6$

Some previous works used other tracers, like LAEs and LBGs, to probe the large-scale structures. But the question of whether the galaxy environment traced by LAEs or LBGs of $z \sim 6$ quasar is overdense or not is still far from clear. Morselli et al. (2014) showed that the environment traced by LBGs around four $z \sim 6$ quasars is overdense in a wide area of ~ 575 arcmin², ~ 3100 cMpc². Conversely, Willott et al. (2005) reported three SDSS quasars at $z \sim 6$ that have no clear signs for LBG overdensity in an area of ~ 30 arcmin² (~ 170 cMpc² at $z \sim 6$).

At $z = 2 - 6$, some observations reported that SMG brightness appears to be correlated with the high-density region of LAEs and LBGs (e.g. Pope et al. 2006; Tamura et al. 2009; Matsuda et al. 2011; Hodge et al. 2013; Umehata et al. 2017; Harikane et al. 2019). Here we compare some individual sources that have previous environment studies traced by LAEs and LBGs on a similar scale. Becker et al. (2018) reported that J0148+0600 field has a highly significant deficit of LAEs. It is roughly one-quarter of background density with ten cMpc (similar size in our survey). But in our millimeter survey, the environment of J0148+0600 has an overdensity of ~ 2.1 ($\sim 3 \times$ the background field).

Conversely, Mazzucchelli et al. (2017) reported no evidence for an overdensity of LAEs in an area of ~ 37 arcmin² centered on the quasar PSO J215-16. We also find no evidence of SMG overdensity in the field of PSO J215-16 in our SHERRY survey. At a similar scale, the different findings may be ascribed to different tracers. These LAEs or LBGs trace the young, dust-poor star-forming galaxies. Nevertheless, some observations and

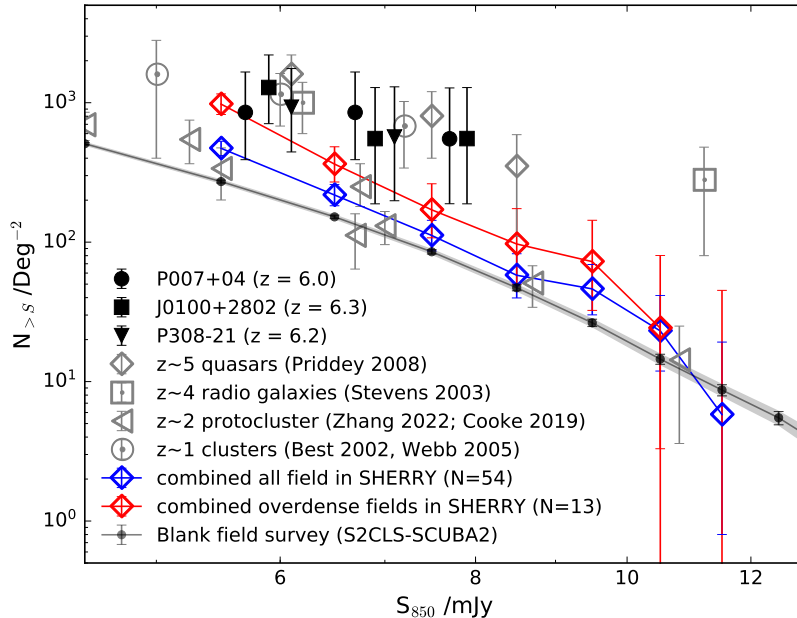


Figure 8. Cumulative number counts of SMGs, in fields centered on (i) luminous high-redshift AGN: $z \sim 5$ optically selected quasars (grey diamonds; Priddey et al. 2008); $z \sim 4$ radio galaxies (grey squares; Stevens et al. 2003); (ii) $z \sim 2$ protoclusters (grey triangles; Zhang et al. 2022; Cooke et al. 2019); (iii) $z \sim 1$ clusters (grey circles; Best 2002; Webb et al. 2005) and (iv) $z \sim 6$ optically selected quasars (this paper, black points and red/blue diamonds). The black line shows the blank-field number counts of SMGs in the previous survey, i.e., SCUBA2 survey for S2CLS field in Geach et al. (2017). The blue line is calculated from our survey’s combined areas of all 54 quasars ($\sim 620 \text{ arcmin}^2$); the red line is from the combined areas of 13 overdense fields around the quasars ($\sim 150 \text{ arcmin}^2$). The black-filled points indicate the three most overdense fields selected from our sample at $z \sim 6$. Points in this work have been corrected for flux boosting and incompleteness.

cosmological simulations indicate that galaxy assembly at high redshift around the quasar might be characterized by galaxies with elevated dust and molecular gas content. (e.g. De Rosa et al. 2011; Yajima et al. 2015). The SMGs trace massive, metal-enriched, and highly obscured objects, which may be a more suited tracer for high redshift overdensities. SMGs, therefore, give us a new perspective on the studies of galaxy environment at high redshift.

4.3. Massive SMGs in proto-clusters

Our SHERRY survey covers 54 $z \sim 6$ quasars (20/54 detected at the sub-mm band, see Li et al. 2020b). We identified 170 SMGs ($> 3.5\sigma$) at 450 and 850 μm , in an area of $\sim 620 \text{ arcmin}^2$. SHERRY represents the first systematic study to probe the environment of $z \sim 6$ quasars in the sub-mm bands. For these SMGs lie $z \sim 6$, their FIR luminosities are $2.2 - 6.4 \times 10^{12} L_{\odot}$, and their star formation rates are $\sim 400 - 1200 M_{\odot} \text{ yr}^{-1}$ (assuming a modified black body SEDs with a typical SMG dust temperature of 35 K, an emissivity index of $\beta = 1.6$ and a Salpeter IMF).

We found that 13/54 fields around $z \sim 6$ quasars exhibit excess above SMG counts compared to a blank field. However, we caution that the other 41/54 quasars

could also reside in the overdense fields, because our survey is not sensitive to the fainter SMGs with $L < 2.0 \times 10^{12} L_{\odot}$. Furthermore, even in an actual dense region of galaxies, the expected number of massive galaxies will not be very large based on the luminosity function.

On the other hand, our SHERRY survey does not provide an accurate redshift determination. Therefore, the SMG overdensity may be diluted over the large cosmological volume. Meyer et al. (2022) presented ALMA observations for three quasar-SMG fields (P231-20 at $z = 6.59$, P308-21 $z = 6.24$ and J0305-3150 $z = 6.61$) selected from our SCUBA2 survey to search for [CII] emission. 12 out of 17 SCUBA2-selected sources are detected with ALMA in the continuum. ALMA detections have offset from the center of pointing due to the large beam of SCUBA2 imaging ($13''$ at $850\mu\text{m}$, e.g., of the order of ALMA field of view, Figure 1 in Meyer et al. 2022). They also search for the [CII] emission lines in six of the continuum-detected sources: four ones in the field of P231-20 ($> 5\sigma$) and two ones around P308-21 ($3-4\sigma$). In the field of PJ231-20, they confirmed a foreground cluster at $z \sim 2.4$. But unfortunately, none of the sources have a photo- z consistent with the background $z \sim 6$ quasars. In the future, more high-resolution imaging and spectroscopic observations

are required for these JCMT-selected protocluster candidates. If we confirm that a significant fraction of the SCUBA-detected galaxies are indeed at the redshift of the quasars (e.g., P007+04, J0100+2802, etc.), we will have striking evidence that some high- z quasars reside in highly overdense regions.

5. SUMMARY

In this paper, we have presented a SCUBA-2 sub-mm survey ‘SHERRY’ of 54 $z \sim 6$ QSOs to study their environment and to search for galaxy protoclusters at the early epoch. The large field of view of JCMT enabled us to identify 170 SMGs ($> 3.5\sigma$) at 450 and 850 μm . SMGs are selected within a distance of ~ 2 arcmins away from the central quasars and have the RMS noise level of ~ 1.2 mJy beam $^{-1}$ in the 850 μm band. This region corresponds to 10 cMpc in diameter, which can trace the typical galaxy protocluster (Chiang et al. 2013). If the SMGs are near the quasar redshifts, their FIR luminosities are $2.2 - 6.4 \times 10^{12} L_{\odot}$ and star formation rates are $\sim 400 - 1200 M_{\odot} \text{yr}^{-1}$. The SMGs discovered in SHERRY provide us with essential candidates for follow-up spectroscopic observations (e.g., [CII]) to secure redshifts and study the first massive large-scale structures in the universe.

We also calculated the SMGs differential and cumulative number counts after correcting for completeness and flux boosting in a combined area of ~ 620 arcmin 2 , which corresponds to ~ 3700 cMpc 2 (~ 76 pMpc 2) at $z \sim 6$. To a 4σ detection (at ~ 5.5 mJy at 850 μm), the SMGs overdensity is $0.68_{-0.19}^{+0.21} (\pm 0.19)$, exceeding ($\sim 1.68 \times$) the source counts of blank sky surveys (S2CLS; Geach et al. 2017). We found 13/54 quasars show SMG overdensities (at ~ 5.5 mJy) in their fields, and the others do not. The combined field of these 13 quasars exceeds the blank field counts with the overdensity to 5.5

mJy of $\delta_{\text{SMG}} \sim 2.46_{-0.55}^{+0.64} (\pm 0.25)$ in the regions of ~ 150 arcmin 2 ; but to the bright end (e.g., 7.5 mJy), the overdensity is not significant. Among them, three (3/13) $z \sim 6$ fields show a significant excess over the blank field, with the overdensity of 2.1 - 5.4 at 5.5 mJy.

We also compared our work and some previous environment studies traced by LAEs and LBGs on a similar scale. These LAEs or LBGs trace the young, dust-poor star-forming galaxies, while the SMGs trace massive, metal-enriched, and highly obscured objects. They may be correlated in the high-density region; therefore, more follow-up spectroscopic works to search for LAEs with JWST, HST, VLT, and ALMA. are required for these fields at a large scale.

1 This work was supported by the National Sci-
 2 ence Foundation of China (NSFC, 11721303,
 3 11991052), the National Key R&D Program of
 4 China (2016YFA0400703), and the NSFC grants No.
 5 11533001. R.W. acknowledge the support from the
 6 Thousand Youth Talents Program of China, NSFC
 7 grants No. 11473004. X.-B. Wu thanks the support from
 8 the National Science Foundation of China (11533001,
 9 11721303). B.V. acknowledges support from the ERC
 10 Advanced Grant 740246 (Cosmic Gas). The authors
 11 wish to recognize and acknowledge the significant cul-
 12 tural role and reverence that the summit of Maunakea
 13 has always had within the indigenous Hawaiian com-
 14 munity. We are most fortunate to have the opportunity
 15 to conduct observations from this mountain. We are
 16 grateful to Paul Hewett, Richard McMahon, Daniel
 17 Mortlock, and Stephen Warren, who supplied the spec-
 18 trum of ULAS J0828+2633. We also thank our support
 19 scientists and telescope schedulers: Harriet Parsons,
 20 Mark G. Rawlings, Iain Coulson, Steven Mairs, and
 21 Jan Wouterloot, for the JCMT observation and data
 22 reduction.

APPENDIX

A. ‘SHERRY’ - SMG CANDIDATES CATALOG AT QUASAR FIELD AT $Z \sim 6$

Here we present SMGs and SMG candidates in the quasar fields at $z \sim 6$. The full catalog includes 170 SMGs selected from 450 and 850 μm images. Column (1) contains the SMG IDs. SMGs are detected above 3.5σ at least in one band, marked as ‘ObjectShortName-SMG+index’. Columns (4) and (7) are the SMG peak flux density in 850 μm and 450 μm bands of SCUBA-2 images; Columns (5) and (8) are signal-to-noise ratio in each band, respectively. Columns (6) and (9) are the deboosted flux density for 850 μm and 450 μm detections calculated from the simulation. Column (10) is the angular distance between SMGs and their central quasar.

Table 2. The catalog of SMGs and its candidates in the quasar nearby fields at $z \sim 6$

Source	RA (J2000) (2)	DEC (J2000) (3)	$S_{\nu,850\mu\text{m}}$ (mJy) (4)	S/N_{850}	$S_{\nu,850\mu\text{m}}^{\text{Deboosted}}$ (mJy) (6)	$S_{\nu,450\mu\text{m}}$ (mJy) (7)	S/N_{450}	$S_{\nu,450\mu\text{m}}^{\text{Deboosted}}$ (mJy) (9)	offset (arcmin) (10)
J0008-0626-SMG1	00h08m24.4s	-06d24m40.5s	6.92±1.32	5.24	6.87±1.86	1.440
J0008-0626-SMG2	00h08m27.1s	-06d28m00.5s	7.11±1.50	4.75	7.08±2.02	45.15±12.29	3.67	43.28±14.26	1.962
P002+32-SMG1	00h09m23.3s	+32d51m44.9s	10.73±1.45	7.39	10.82±2.10	2.193
P002+32-SMG2	00h09m34.1s	+32d53m12.9s	5.86±1.25	4.70	5.65±1.69	1.144
P002+32-SMG3	00h09m27.1s	+32d53m12.9s	4.96±1.34	3.70	4.48±1.52	1.555
P002+32-SMG4	00h09m33.1s	+32d54m04.9s	5.14±1.43	3.60	4.72±1.63	1.893
P002+32-SMG5	00h09m35.6s	+32d51m16.9s	4.38±1.22	3.59	3.67±1.25	1.334
P002+32-SMG6	00h09m35.6s	+32d53m44.9s	4.79±1.34	3.58	4.23±1.45	1.805
P002+32-SMG7	00h09m27.7s	+32d51m32.9s	4.30±1.21	3.54	3.56±1.22	1.228
P007+04-SMG1	00h28m07.4s	+04d57m41.7s	10.79±1.08	9.95	10.87±1.78	0.334
P007+04-SMG2	00h28m05.2s	+04d56m53.7s	7.71±1.12	6.86	7.77±1.79	0.630
P007+04-SMG3	00h28m07.9s	+04d57m17.7s	6.84±1.10	6.24	6.88±1.76	0.360
P007+04-SMG4	00h28m05.7s	+04d56m29.7s	4.60±1.17	3.94	4.11±1.33	0.955
P007+04-SMG5	00h28m13.5s	+04d58m09.7s	5.23±1.43	3.65	4.97±1.71	1.888
P007+04-SMG6	00h28m08.7s	+04d59m01.7s	4.18±1.17	3.56	3.54±1.21	1.687
P007+04-SMG7	00h28m02.3s	+04d59m01.7s	4.30±1.22	3.51	3.70±1.28	1.925
J0100+2802-AGN	01h00m12.6s	+28d02m25.8s	4.09±1.13	3.63	3.34±1.11	0.076
J0100+2802-SMG1	01h00m13.9s	+28d00m25.8s	9.94±1.47	6.77	10.00±2.08	2.013
J0100+2802-SMG2	01h00m09.0s	+28d04m13.8s	8.00±1.32	6.05	8.03±1.95	2.050
J0100+2802-SMG3	01h00m14.2s	+28d02m53.8s	5.48±1.12	4.88	5.18±1.50	0.556
J0100+2802-SMG4	01h00m21.4s	+28d02m21.8s	5.99±1.40	4.29	5.81±1.79	2.116
J0100+2802-SMG5	01h00m17.5s	+28d03m17.8s	4.11±1.16	3.53	3.37±1.14	1.426
J0148+0600-AGN	01h48m37.5s	+06d00m20.0s	5.28±1.19	4.45	4.78±1.45	0.000
J0148+0600-SMG1	01h48m37.8s	+05d58m28.0s	6.83±1.49	4.57	6.76±2.05	1.868
J0148+0600-SMG2	01h48m40.0s	+05d59m36.0s	5.43±1.27	4.27	4.98±1.55	0.950
J0148+0600-SMG3	01h48m39.4s	+06d00m44.0s	5.18±1.22	4.23	4.66±1.45	0.617

Table 2 continued

Table 2 (continued)

Source	RA (J2000) (2)	DEC (J2000) (3)	$S_{\nu,850\mu\text{m}}$ (mJy) (4)	S/N_{850}	$S_{\nu,850\mu\text{m}}^{\text{Deboosted}}$ (mJy) (6)	$S_{\nu,450\mu\text{m}}$ (mJy) (7)	S/N_{450}	$S_{\nu,450\mu\text{m}}^{\text{Deboosted}}$ (mJy) (9)	offset (arcmin) (10)
J0148+0600-SMG4	01h48m42.9s	+06d01m08.0s	5.86±1.43	4.11	5.56±1.79	1.561
J0148+0600-SMG5	01h48m30.8s	+06d00m12.0s	5.23±1.42	3.67	4.72±1.61	1.681
J0148+0600-SMG6	01h48m41.0s	+06d01m20.0s	4.79±1.32	3.64	4.12±1.39	1.326
P036+03-AGN	02h26m02.8s	+03d02m59.4s	5.47±1.01	5.42	5.31±1.48	0.000
P036+03-SMG1	02h26m02.6s	+03d04m19.4s	11.32±1.08	10.49	11.39±1.77	1.335
P036+03-SMG2	02h25m58.0s	+03d03m47.4s	6.33±1.06	6.00	6.33±1.68	1.444
P036+03-SMG3	02h25m58.6s	+03d01m47.4s	4.79±1.15	4.16	4.44±1.39	1.607
P036+03-SMG4	02h26m10.0s	+03d02m43.4s	5.20±1.31	3.96	4.96±1.62	1.822
P036+03-SMG5	02h26m02.6s	+03d03m47.4s	4.04±1.04	3.89	3.43±1.10	53.42±17.57	3.04	39.99±14.54	0.803
P036+03-SMG6	02h26m05.0s	+03d04m27.4s	4.40±1.16	3.79	3.93±1.29	1.561
J0305-3150-AGN	03h05m18.2s	-31d50m55.8s	8.43±1.08	7.78	8.50±1.77	0.078
J0305-3150-SMG1	03h05m22.3s	-31d49m47.8s	6.50±1.30	5.00	6.49±1.83	1.579
J0305-3150-SMG2	03h05m12.5s	-31d51m23.8s	5.27±1.11	4.76	5.00±1.47	1.413
J0305-3150-SMG3	03h05m26.0s	-31d49m59.8s	5.93±1.45	4.08	5.83±1.86	2.244
J0305-3150-SMG4	03h05m07.8s	-31d50m51.8s	4.41±1.23	3.58	3.86±1.31	2.512
P055-00-SMG1	03h41m44.2s	-00d48m28.6s	6.38±1.31	4.86	6.21±1.79	0.657
P055-00-SMG2	03h41m40.8s	-00d47m12.6s	4.84±1.25	3.88	4.21±1.35	1.035
P055-00-SMG3	03h41m43.2s	-00d47m28.6s	4.86±1.28	3.80	4.23±1.38	0.806
P055-00-SMG4	03h41m38.1s	-00d50m04.6s	5.39±1.49	3.61	4.97±1.69	2.087
P055-00-SMG5	03h41m38.1s	-00d46m36.6s	4.66±1.33	3.51	3.97±1.36	1.853
P056-16-SMG1	03h46m58.0s	-16d29m44.8s	5.85±1.05	5.55	5.81±1.51	1.688
P056-16-SMG2	03h46m58.0s	-16d28m08.8s	5.08±1.02	4.96	4.95±1.40	1.336
P056-16-SMG3	03h46m48.3s	-16d27m04.8s	4.16±1.09	3.81	3.84±1.27	1.936
P060+24-SMG1	04h02m08.4s	+24d51m32.5s	6.90±1.28	5.39	6.83±1.86	1.329
P060+24-SMG2	04h02m07.2s	+24d50m08.5s	6.78±1.46	4.65	6.69±1.97	2.054
P060+24-SMG3	04h02m19.8s	+24d52m20.5s	4.88±1.34	3.63	4.32±1.46	1.803
P060+24-SMG4	04h02m12.2s	+24d52m48.5s	4.41±1.23	3.57	3.68±1.25	1.447
P065-19-SMG1	04h22m01.7s	-19d29m28.6s	6.22±1.22	5.09	6.20±1.73	2.001

Table 2 continued

Table 2 (continued)

Source	RA (J2000)	DEC (J2000)	$S_{\nu,850\mu\text{m}}$ (mJy)	S/N_{850}	$S_{\nu,850\mu\text{m}}^{\text{Deboosted}}$ (mJy)	$S_{\nu,450\mu\text{m}}$ (mJy)	S/N_{450}	$S_{\nu,450\mu\text{m}}^{\text{Deboosted}}$ (mJy)	offset (arcmin)
(1)	(2)	(3)	(4)	(5)	(6)	(7)	(8)	(9)	(10)
P065-19-SMG2	04h21m56.9s	-19d26m28.6s	5.13±1.04	4.95	4.95±1.45	1.619
P065-19-SMG3	04h22m05.4s	-19d26m48.6s	4.28±1.08	3.95	3.81±1.23	1.079
P065-19-SMG4	04h22m09.3s	-19d26m20.6s	4.98±1.32	3.78	4.74±1.60	2.160
P089-15-AGN	05h59m46.4s	-15d35m00.1s	3.56±1.17	3.05	2.60±0.96	0.000
P089-15-SMG1	05h59m42.8s	-15d34m56.1s	6.28±1.17	5.36	6.13±1.65	100.56±31.85	3.16	76.23±27.15	0.902
P089-15-SMG2	05h59m53.3s	-15d34m20.1s	5.64±1.46	3.86	5.37±1.75	113.21±36.11	3.13	93.10±33.58	1.854
J0810+5105-SMG1	08h10m57.6s	+51d04m32.1s	4.85±1.22	3.98	4.34±1.38	1.416
J0810+5105-SMG2	08h10m52.1s	+51d04m40.1s	4.65±1.26	3.69	4.06±1.35	1.132
J0810+5105-SMG3	08h11m04.4s	+51d04m52.1s	4.70±1.28	3.69	4.13±1.37	2.670
J0810+5105-SMG4	08h10m47.5s	+51d06m36.1s	4.76±1.34	3.55	4.22±1.44	1.938
J0828+2633-SMG1	08h28m09.5s	+26d34m39.5s	7.12±1.31	5.45	7.10±1.88	1.215
J0828+2633-SMG2	08h28m15.1s	+26d31m55.5s	5.68±1.45	3.92	5.41±1.75	2.049
J0828+2633-SMG3	08h28m15.4s	+26d33m03.5s	4.41±1.23	3.58	3.71±1.24	1.012
J0835+3217-SMG1	08h35m33.3s	+32d19m08.6s	5.89±1.42	4.15	5.65±1.75	2.278
J0835+3217-SMG2	08h35m34.9s	+32d18m00.6s	5.79±1.49	3.89	5.52±1.78	2.291
J0835+3217-SMG3	08h35m32.1s	+32d17m56.6s	5.08±1.35	3.78	4.59±1.49	54.28±17.32	3.13	43.16±15.51	1.579
J0839+0015-SMG1	08h39m57.7s	+00d16m50.2s	4.75±1.28	3.72	4.18±1.37	1.110
J0842+1218-SMG1	08h42m27.4s	+12d19m34.5s	8.49±1.36	6.24	8.53±2.05	0.875
J0842+1218-SMG2	08h42m25.8s	+12d18m50.5s	6.15±1.31	4.68	5.91±1.74	51.62±13.79	3.74	44.90±14.33	0.887
J0850+3246-SMG1	08h50m41.9s	+32d45m11.9s	6.08±1.39	4.38	5.86±1.82	2.253
J0850+3246-SMG2	08h50m54.3s	+32d46m51.9s	4.79±1.35	3.54	4.12±1.41	1.508
P135+16-AGN	09h01m32.6s	+16d15m06.8s	5.16±1.34	3.86	4.49±1.44	0.000
P159-02-SMG1	10h36m48.3s	-02d31m45.8s	6.61±1.38	4.80	6.47±1.89	1.705
P159-02-SMG2	10h36m58.7s	-02d31m49.8s	5.51±1.49	3.69	5.05±1.70	1.388
J1048-0109-AGN	10h48m19.0s	-01d09m40.2s	4.56±1.17	3.89	3.99±1.26	0.000
J1048-0109-SMG1	10h48m20.4s	-01d11m12.2s	7.74±1.37	5.66	7.79±1.91	1.569
J1048-0109-SMG2	10h48m23.0s	-01d09m00.2s	5.61±1.33	4.23	5.37±1.63	1.202
J1048-0109-SMG3	10h48m12.1s	-01d08m20.2s	4.97±1.39	3.59	4.54±1.51	2.187

Table 2 continued

Table 2 (continued)

Source	RA (J2000)	DEC (J2000)	$S_{\nu,850\mu\text{m}}$ (mJy)	S/N_{850}	$S_{\nu,850\mu\text{m}}^{\text{Deboosted}}$ (mJy)	$S_{\nu,450\mu\text{m}}$ (mJy)	S/N_{450}	$S_{\nu,450\mu\text{m}}^{\text{Deboosted}}$ (mJy)	offset (arcmin)
(1)	(2)	(3)	(4)	(5)	(6)	(7)	(8)	(9)	(10)
J1048-0109-SMG4	10h48m22.8s	-01d10m20.2s	4.59±1.30	3.53	4.03±1.35	1.147
P167-13-SMG1	11h10m30.7s	-13d31m05.5s	5.40±1.38	3.92	5.03±1.62	1.567
P167-13-SMG2	11h10m29.6s	-13d29m09.5s	4.31±1.21	3.56	3.58±1.20	1.250
J1143+3808-SMG1	11h43m46.0s	+38d07m48.7s	6.19±1.49	4.15	5.85±1.83	2.060
J1143+3808-SMG2	11h43m37.6s	+38d09m36.7s	5.86±1.43	4.10	5.44±1.70	1.146
J1148+0702-SMG1	11h48m00.6s	+07d02m44.3s	10.02±1.33	7.54	10.07±1.99	0.901
J1148+0702-SMG2	11h48m05.4s	+07d02m48.3s	4.87±1.36	3.58	4.22±1.39	0.856
J1152+0055-SMG1	11h52m12.9s	+00d55m48.6s	7.68±1.23	6.23	7.62±1.84	2.077
J1152+0055-SMG2	11h52m23.4s	+00d56m28.6s	4.16±1.13	3.69	3.48±1.17	1.018
J1152+0055-SMG3	11h52m19.1s	+00d57m00.6s	4.19±1.15	3.65	3.52±1.20	1.498
J1152+0055-SMG4	11h52m21.0s	+00d56m28.6s	3.98±1.09	3.65	3.24±1.09	0.869
J1152+0055-SMG5	11h52m28.2s	+00d56m48.6s	5.32±1.50	3.56	5.01±1.76	2.108
J1205+0505-SMG1	12h05m06.4s	+00d01m03.9s	7.49±1.31	5.72	7.49±1.85	1.569
J1205+0505-SMG2	12h05m08.0s	+00d00m03.9s	5.12±1.32	3.89	4.69±1.49	0.907
J1207+0630-SMG1	12h07m36.3s	+06d31m46.0s	6.03±1.30	4.62	5.85±1.72	31.86±10.23	3.11	25.61±9.28	1.622
J1207+0630-SMG2	12h07m37.9s	+06d30m50.0s	4.47±1.24	3.59	3.73±1.22	0.680
P183+05-AGN	12h12m27.2s	+05d05m29.4s	9.03±1.30	6.93	9.13±2.03	0.094
P183+05-SMG1	12h12m23.4s	+05d05m33.4s	4.77±1.34	3.55	4.06±1.37	0.870
P183+05-SMG2	12h12m29.6s	+05d06m13.4s	4.93±1.42	3.48	4.30±1.48	33.47±8.93	3.75	28.82±9.26	0.945
P183-12-AGN	12h13m11.7s	-12d46m03.5s	4.08±1.14	3.59	3.25±1.09	0.000
P183-12-SMG1	12h13m13.9s	-12d46m39.5s	9.48±1.21	7.83	9.48±1.86	0.812
P183-12-SMG2	12h13m14.8s	-12d45m11.5s	4.53±1.25	3.62	3.89±1.32	1.147
P184+01-AGN	12h17m21.8s	+01d31m30.4s	3.67±1.12	3.26	2.76±0.97	0.240
P184+01-SMG1	12h17m26.6s	+01d31m14.4s	5.85±1.29	4.54	5.61±1.69	43.03±11.41	3.77	39.76±12.68	1.413
P184+01-SMG2	12h17m18.6s	+01d30m50.4s	4.96±1.17	4.23	4.48±1.39	1.094
P184+01-SMG3	12h17m20.0s	+01d33m10.4s	4.55±1.24	3.67	3.91±1.31	1.504
P187+04-AGN	12h29m12.3s	+04d19m23.6s	3.81±1.25	3.04	2.79±1.03	0.211
P187+04-SMG1	12h29m09.7s	+04d20m47.6s	6.88±1.35	5.09	6.79±1.92	1.592

Table 2 continued

Table 2 (continued)

Source	RA (J2000)	DEC (J2000)	$S_{\nu,850\mu\text{m}}$ (mJy)	S/N ₈₅₀	$S_{\nu,850\mu\text{m}}^{\text{Deboosted}}$ (mJy)	$S_{\nu,450\mu\text{m}}$ (mJy)	S/N ₄₅₀	$S_{\nu,450\mu\text{m}}^{\text{Deboosted}}$ (mJy)	offset (arcmin)
(1)	(2)	(3)	(4)	(5)	(6)	(7)	(8)	(9)	(10)
P187+04-SMG2	12h29m13.1s	+04d20m03.6s	5.35±1.24	4.30	4.84±1.46	0.600
J1243+2529-SMG1	12h43m43.4s	+25d28m15.8s	7.94±1.45	5.46	8.01±2.17	1.314
J1243+2529-SMG2	12h43m42.8s	+25d30m19.8s	5.55±1.40	3.95	5.06±1.61	1.067
J1257+6349-SMG1	12h57m59.3s	+63d50m29.1s	5.11±1.10	4.65	4.84±1.39	0.978
J1257+6349-SMG2	12h57m46.6s	+63d49m49.1s	5.29±1.20	4.42	5.07±1.50	35.14±9.23	3.81	32.30±10.30	2.728
P210+27-SMG1	14h01m53.0s	+27d49m10.9s	9.33±1.30	7.15	9.45±2.13	1.487
P210+27-SMG2	14h01m46.1s	+27d49m54.9s	5.02±1.20	4.19	4.46±1.41	0.449
P210+27-SMG3	14h01m45.5s	+27d48m46.9s	4.75±1.18	4.03	4.09±1.31	38.46±10.43	3.69	32.77±10.57	0.919
P210+27-SMG4	14h01m49.4s	+27d49m38.9s	4.47±1.19	3.74	3.70±1.22	0.532
P210+27-SMG5	14h01m39.8s	+27d50m18.9s	5.29±1.49	3.54	4.84±1.71	2.022
P210+27-SMG6	14h01m40.1s	+27d48m54.9s	4.99±1.42	3.51	4.43±1.56	1.928
P210+27-SMG7	14h01m42.8s	+27d49m38.9s	4.47±1.28	3.50	3.70±1.28	1.133
P210+40-SMG1	14h03m00.6s	+40d23m59.1s	5.51±1.27	4.34	5.18±1.57	1.490
P210+40-SMG2	14h02m55.3s	+40d24m15.1s	4.69±1.24	3.77	4.04±1.31	0.266
P210-12-AGN	14h03m29.8s	-12d00m34.1s	3.56±1.16	3.07	2.61±0.96	0.136
P210-12-SMG1	14h03m31.4s	-12d01m06.1s	5.71±1.21	4.70	5.45±1.58	0.763
P210-12-SMG2	14h03m28.2s	-11d58m50.1s	5.41±1.40	3.85	5.06±1.64	1.755
P215-16-AGN	14h20m36.2s	-16d02m30.2s	16.85±1.10	15.36	16.96±1.90	26.93±7.78	3.46	21.66±7.26	0.000
P215-16-SMG1	14h20m35.4s	-16d03m34.2s	6.08±1.20	5.07	5.97±1.73	1.087
P215-16-SMG2	14h20m37.1s	-16d01m58.2s	4.97±1.14	4.36	4.54±1.40	27.51±7.92	3.47	22.46±7.53	0.572
P215-16-SMG3	14h20m35.7s	-16d00m50.2s	5.13±1.30	3.95	4.76±1.56	1.672
P215-16-SMG4	14h20m34.0s	-16d02m02.2s	3.97±1.10	3.60	3.17±1.06	0.725
P215-16-SMG5	14h20m39.6s	-16d02m02.2s	4.19±1.19	3.54	3.47±1.19	27.06±8.28	3.27	21.87±7.65	0.954
P215+26-SMG1	14h21m42.0s	+26d33m09.0s	6.83±1.22	5.59	6.75±1.79	1.236
P215+26-SMG2	14h21m42.3s	+26d33m45.0s	5.79±1.28	4.51	5.52±1.65	1.814
P215+26-SMG3	14h21m43.2s	+26d31m33.0s	4.56±1.21	3.76	3.89±1.26	33.35±10.85	3.07	24.92±9.01	0.400
P215+26-SMG4	14h21m50.1s	+26d33m01.0s	5.11±1.43	3.57	4.62±1.57	2.019
P215+26-SMG5	14h21m37.9s	+26d32m41.0s	4.45±1.26	3.53	3.74±1.26	1.529

Table 2 continued

Table 2 (continued)

Source	RA (J2000)	DEC (J2000)	$S_{\nu,850\mu\text{m}}$ (mJy)	S/N_{850}	$S_{\nu,850\mu\text{m}}^{\text{Deboosted}}$ (mJy)	$S_{\nu,450\mu\text{m}}$ (mJy)	S/N_{450}	$S_{\nu,450\mu\text{m}}^{\text{Deboosted}}$ (mJy)	offset (arcmin)
(1)	(2)	(3)	(4)	(5)	(6)	(7)	(8)	(9)	(10)
P217-16-SMG1	14h28m21.3s	-16d01m15.3s	5.81±1.38	4.22	5.54±1.73	1.467
P217-16-SMG2	14h28m20.2s	-16d02m15.3s	4.52±1.22	3.69	3.79±1.24	0.543
P217-07-AGN	14h31m40.7s	-07d24m47.5s	6.03±1.17	5.16	5.86±1.61	0.095
P217-07-SMG1	14h31m38.0s	-07d24m03.5s	4.97±1.22	4.08	4.53±1.40	0.900
P231-20-AGN	15h26m37.8s	-20d50m00.7s	7.99±1.22	6.53	8.06±1.99	80.31±19.97	4.02	71.00±21.54	0.000
P231-20-SMG1	15h26m39.8s	-20d51m12.7s	6.01±1.35	4.46	5.77±1.77	1.300
P231-20-SMG2	15h26m38.4s	-20d50m44.7s	5.40±1.26	4.27	4.98±1.56	0.747
P231-20-SMG3	15h26m38.9s	-20d51m36.7s	5.57±1.39	4.00	5.22±1.70	1.625
P239-07-SMG1	15h58m56.0s	-07d23m57.6s	4.62±1.31	3.53	4.02±1.37	1.293
J1609+3041-AGN	16h09m36.9s	+30d41m47.6s	4.09±1.17	3.50	3.27±1.11	0.078
J1609+3041-SMG1	16h09m44.7s	+30d41m51.6s	7.19±1.44	5.01	7.16±2.00	25.56±8.27	3.09	20.53±7.45	1.862
J1609+3041-SMG2	16h09m32.3s	+30d43m43.6s	5.40±1.35	3.99	5.02±1.62	2.297
J1609+3041-SMG3	16h09m42.5s	+30d43m03.6s	4.90±1.28	3.83	4.37±1.44	1.828
J1609+3041-SMG4	16h09m31.4s	+30d42m43.6s	4.63±1.28	3.62	4.01±1.36	1.744
P247+24-AGN	16h29m11.8s	+24d07m35.6s	6.76±1.13	5.98	6.77±1.72	0.161
P247+24-SMG1	16h29m03.7s	+24d08m39.6s	6.65±1.32	5.05	6.65±1.83	2.146
P247+24-SMG2	16h29m05.1s	+24d06m07.6s	6.65±1.39	4.80	6.66±1.89	2.169
P308-21-AGN	20h32m09.7s	-21d14m02.3s	4.23±1.09	3.86	3.59±1.17	0.072
P308-21-SMG1	20h32m15.9s	-21d13m02.3s	9.92±1.37	7.27	10.00±2.00	1.804
P308-21-SMG2	20h32m10.8s	-21d12m54.3s	6.13±1.22	5.02	6.02±1.71	60.37±18.27	3.30	49.54±17.18	1.153
P308-21-SMG3	20h32m05.1s	-21d15m10.3s	5.03±1.19	4.23	4.65±1.44	1.662
P308-21-SMG4	20h32m06.8s	-21d14m10.3s	4.30±1.11	3.88	3.70±1.20	0.798
P308-21-SMG5	20h32m08.8s	-21d16m02.3s	4.72±1.30	3.64	4.27±1.45	62.30±20.10	3.10	52.20±19.02	2.020
P308-21-SMG6	20h32m08.8s	-21d13m10.3s	4.32±1.19	3.64	3.73±1.26	0.913
P308-21-SMG7	20h32m13.7s	-21d15m06.3s	4.50±1.24	3.63	3.97±1.35	1.415
P308-21-SMG8	20h32m13.7s	-21d14m26.3s	4.17±1.18	3.55	3.51±1.20	1.012
J2100-1715-SMG1	21h01m00.0s	-17d14m02.5s	5.21±1.20	4.34	5.05±1.55	1.739
J2100-1715-SMG2	21h00m58.1s	-17d16m58.5s	4.68±1.12	4.18	4.40±1.39	1.719

Table 2 continued

Table 2 (continued)

Source	RA (J2000)	DEC (J2000)	$S_{\nu,850\mu\text{m}}$ (mJy)	S/N ₈₅₀	$S_{\nu,850\mu\text{m}}^{\text{Deboosted}}$ (mJy)	$S_{\nu,450\mu\text{m}}$ (mJy)	S/N ₄₅₀	$S_{\nu,450\mu\text{m}}^{\text{Deboosted}}$ (mJy)	offset (arcmin)
(1)	(2)	(3)	(4)	(5)	(6)	(7)	(8)	(9)	(10)
J2100-1715-SMG3	21h00m53.6s	-17d15m14.5s	3.73±0.95	3.91	3.18±1.04	0.507
J2100-1715-SMG4	21h00m58.4s	-17d13m42.5s	4.76±1.22	3.89	4.52±1.49	1.807
P323+12-SMG1	21h32m35.2s	+12d16m27.1s	5.78±1.24	4.68	5.66±1.65	1.492
P323+12-SMG2	21h32m25.7s	+12d18m43.1s	4.63±1.24	3.72	4.24±1.42	2.261
P323+12-SMG3	21h32m28.7s	+12d16m39.1s	4.46±1.22	3.65	4.03±1.37	1.862
P333+26-AGN	22h15m57.6s	+26d06m33.3s	3.83±1.04	3.69	3.07±1.03	0.067
P333+26-SMG1	22h16m05.9s	+26d07m21.3s	8.11±1.27	6.39	8.12±1.89	2.252
P333+26-SMG2	22h16m04.4s	+26d07m13.3s	5.70±1.20	4.74	5.54±1.68	1.858
P333+26-SMG3	22h16m03.8s	+26d07m53.3s	4.79±1.19	4.01	4.37±1.43	95.40±22.93	4.16	92.95±27.69	2.095
P333+26-SMG4	22h15m50.5s	+26d05m33.3s	4.65±1.22	3.82	4.18±1.41	2.011
P333+26-SMG5	22h15m54.3s	+26d07m45.3s	4.22±1.13	3.73	3.60±1.22	1.507
P338+29-SMG1	22h32m58.5s	+29d29m44.1s	6.50±1.45	4.48	6.31±1.92	1.162
P338+29-SMG2	22h32m54.5s	+29d32m08.1s	6.16±1.43	4.30	5.88±1.83	1.607
P338+29-SMG3	22h32m56.4s	+29d31m00.1s	4.70±1.32	3.57	3.94±1.36	0.558
P340-18-SMG1	22h40m46.9s	-18d39m43.8s	4.91±1.03	4.79	4.64±1.36	0.774
P340-18-SMG2	22h40m48.6s	-18d39m11.8s	4.10±1.03	3.97	3.57±1.14	0.639
P340-18-SMG3	22h40m49.1s	-18d37m39.8s	4.93±1.31	3.76	4.66±1.56	2.077
P340-18-SMG4	22h40m50.0s	-18d40m23.8s	3.86±1.05	3.66	3.24±1.08	0.667
J2348-3054-AGN	23h48m34.3s	-30d54m10.1s	5.88±1.06	5.52	5.81±1.51	0.000
J2348-3054-SMG1	23h48m40.8s	-30d53m46.1s	5.02±1.27	3.96	4.78±1.50	1.680
P359-06-SMG1	23h56m30.7s	-06d23m35.2s	4.50±1.14	3.96	3.95±1.28	0.900
P359-06-SMG2	23h56m28.3s	-06d24m07.2s	5.08±1.31	3.88	4.74±1.57	1.706
P359-06-SMG3	23h56m27.5s	-06d22m31.2s	4.35±1.16	3.76	3.73±1.24	1.548
P359-06-SMG4	23h56m37.4s	-06d21m47.2s	4.95±1.33	3.73	4.56±1.55	1.566

REFERENCES

- Ajiki, M., Taniguchi, Y., Murayama, T., et al. 2006, PASJ, 58, 499, doi: [10.1093/pasj/58.3.499](https://doi.org/10.1093/pasj/58.3.499)
- Bañados, E., Venemans, B. P., Decarli, R., et al. 2016, ApJS, 227, 11, doi: [10.3847/0067-0049/227/1/11](https://doi.org/10.3847/0067-0049/227/1/11)
- Bañados, E., Venemans, B. P., Morganson, E., et al. 2014, AJ, 148, 14, doi: [10.1088/0004-6256/148/1/14](https://doi.org/10.1088/0004-6256/148/1/14)
- Becker, G. D., Davies, F. B., Furlanetto, S. R., et al. 2018, ApJ, 863, 92, doi: [10.3847/1538-4357/aacc73](https://doi.org/10.3847/1538-4357/aacc73)
- Best, P. N. 2002, MNRAS, 336, 1293, doi: [10.1046/j.1365-8711.2002.05896.x](https://doi.org/10.1046/j.1365-8711.2002.05896.x)
- Carnall, A. C., Shanks, T., Chehade, B., et al. 2015, MNRAS: Letters, 451, L16, doi: [10.1093/mnras/451/1/L16](https://doi.org/10.1093/mnras/451/1/L16)
- Casey, C. M., Chen, C.-C., Cowie, L. L., et al. 2013, MNRAS, 436, 1919, doi: [10.1093/mnras/stt1673](https://doi.org/10.1093/mnras/stt1673)
- Champagne, J. B., Decarli, R., Casey, C. M., et al. 2018, ApJ, 867, 153, doi: [10.3847/1538-4357/aae396](https://doi.org/10.3847/1538-4357/aae396)
- Chapin, E. L., Berry, D. S., Gibb, A. G., et al. 2013, MNRAS, 430, 2545, doi: [10.1093/mnras/stt052](https://doi.org/10.1093/mnras/stt052)
- Chen, C.-C., Cowie, L. L., Barger, A. J., et al. 2013, ApJ, 776, 131, doi: [10.1088/0004-637X/776/2/131](https://doi.org/10.1088/0004-637X/776/2/131)
- Chen, C.-C., Cowie, L. L., Wang, W.-H., Barger, A. J., & Williams, J. P. 2011, ApJ, 733, 64, doi: [10.1088/0004-637X/733/1/64](https://doi.org/10.1088/0004-637X/733/1/64)
- Chiang, Y.-K., Overzier, R., & Gebhardt, K. 2013, ApJ, 779, 127, doi: [10.1088/0004-637X/779/2/127](https://doi.org/10.1088/0004-637X/779/2/127)
- Chiang, Y.-K., Overzier, R. A., Gebhardt, K., & Henriques, B. 2017, ApJ, 844, L23, doi: [10.3847/2041-8213/aa7e7b](https://doi.org/10.3847/2041-8213/aa7e7b)
- Cooke, E. A., Smail, I., Stach, S. M., et al. 2019, MNRAS, 486, 3047, doi: [10.1093/mnras/stz955](https://doi.org/10.1093/mnras/stz955)
- Costa, T., Sijacki, D., Trenti, M., & Haehnelt, M. G. 2014, MNRAS, 439, 2146, doi: [10.1093/mnras/stu101](https://doi.org/10.1093/mnras/stu101)
- Cowie, L. L., Barger, A. J., & Kneib, J.-P. 2002, AJ, 123, 2197, doi: [10.1086/339978](https://doi.org/10.1086/339978)
- De Breuck, C., Bertoldi, F., Carilli, C., et al. 2004, A&A, 424, 1, doi: [10.1051/0004-6361/20035885](https://doi.org/10.1051/0004-6361/20035885)
- De Rosa, G., Decarli, R., Walter, F., et al. 2011, ApJ, 739, 56, doi: [10.1088/0004-637X/739/2/56](https://doi.org/10.1088/0004-637X/739/2/56)
- Decarli, R., Walter, F., Venemans, B. P., et al. 2017, Nature, 545, 457, doi: [10.1038/nature22358](https://doi.org/10.1038/nature22358)
- Dempsey, J. T., Friberg, P., Jenness, T., et al. 2013, MNRAS, 430, 2534, doi: [10.1093/mnras/stt090](https://doi.org/10.1093/mnras/stt090)
- Eales, S., Lilly, S., Webb, T., et al. 2000, AJ, 120, 2244, doi: [10.1086/316823](https://doi.org/10.1086/316823)
- Fan, X., Strauss, M. A., Richards, G. T., et al. 2006, AJ, 131, 1203, doi: [10.1086/500296](https://doi.org/10.1086/500296)
- Geach, J. E., Dunlop, J. S., Halpern, M., et al. 2017, MNRAS, 465, 1789, doi: [10.1093/mnras/stw2721](https://doi.org/10.1093/mnras/stw2721)
- Gehrels, N. 1986, ApJ, 303, 336, doi: [10.1086/164079](https://doi.org/10.1086/164079)
- Goto, T., Utsumi, Y., Kikuta, S., et al. 2017, MNRAS, 470, L117, doi: [10.1093/mnrasl/slx088](https://doi.org/10.1093/mnrasl/slx088)
- Greve, T. R., Stern, D., Ivison, R. J., et al. 2007, MNRAS, 382, 48, doi: [10.1111/j.1365-2966.2007.12292.x](https://doi.org/10.1111/j.1365-2966.2007.12292.x)
- Harikane, Y., Ouchi, M., Ono, Y., et al. 2019, arXiv e-prints, arXiv:1902.09555, <https://arxiv.org/abs/1902.09555>
- Hatsukade, B., Kohno, K., Umehata, H., et al. 2016, PASJ, 68, 36, doi: [10.1093/pasj/psw026](https://doi.org/10.1093/pasj/psw026)
- Hickox, R. C., Wardlow, J. L., Smail, I., et al. 2012, MNRAS, 421, 284, doi: [10.1111/j.1365-2966.2011.20303.x](https://doi.org/10.1111/j.1365-2966.2011.20303.x)
- Hodge, J. A., Karim, A., Smail, I., et al. 2013, ApJ, 768, 91, doi: [10.1088/0004-637X/768/1/91](https://doi.org/10.1088/0004-637X/768/1/91)
- Jiang, L., Fan, X., Annis, J., et al. 2008, AJ, 135, 1057, doi: [10.1088/0004-6256/135/3/1057](https://doi.org/10.1088/0004-6256/135/3/1057)
- Knudsen, K. K., van der Werf, P. P., & Kneib, J. P. 2008, MNRAS, 384, 1611, doi: [10.1111/j.1365-2966.2007.12820.x](https://doi.org/10.1111/j.1365-2966.2007.12820.x)
- Li, Q., Wang, R., Fan, X., et al. 2020a, ApJ, 900, 12, doi: [10.3847/1538-4357/aba52d](https://doi.org/10.3847/1538-4357/aba52d)
- . 2020b, ApJ, 900, 12, doi: [10.3847/1538-4357/aba52d](https://doi.org/10.3847/1538-4357/aba52d)
- Matsuda, Y., Smail, I., Geach, J. E., et al. 2011, MNRAS, 416, 2041, doi: [10.1111/j.1365-2966.2011.19179.x](https://doi.org/10.1111/j.1365-2966.2011.19179.x)
- Matsuoka, Y., Onoue, M., Kashikawa, N., et al. 2016, ApJ, 828, 1, doi: [10.3847/0004-637X/828/1/26](https://doi.org/10.3847/0004-637X/828/1/26)
- Mazzucchelli, C., Bañados, E., Decarli, R., et al. 2017, ApJ, 834, 83, doi: [10.3847/1538-4357/834/1/83](https://doi.org/10.3847/1538-4357/834/1/83)
- Meyer, R. A., Decarli, R., Walter, F., et al. 2022, ApJ, 927, 141, doi: [10.3847/1538-4357/ac4f67](https://doi.org/10.3847/1538-4357/ac4f67)
- Morselli, L., Mignoli, M., Gilli, R., et al. 2014, A&A, 568, A1, doi: [10.1051/0004-6361/201423853](https://doi.org/10.1051/0004-6361/201423853)
- Mortlock, D. J., Warren, S. J., Venemans, B. P., et al. 2011, Nature, 474, 616, doi: [10.1038/nature10159](https://doi.org/10.1038/nature10159)
- Murdoch, H. S., Crawford, D. F., & Jauncey, D. L. 1973, ApJ, 183, 1, doi: [10.1086/152202](https://doi.org/10.1086/152202)
- Omont, A., Willott, C. J., Beelen, A., et al. 2013, A&A, 552, A43, doi: [10.1051/0004-6361/201221006](https://doi.org/10.1051/0004-6361/201221006)
- Ota, K., Venemans, B. P., Taniguchi, Y., et al. 2018, ApJ, 856, 109, doi: [10.3847/1538-4357/aab35b](https://doi.org/10.3847/1538-4357/aab35b)
- Overzier, R. A., Shu, X., Zheng, W., et al. 2009, ApJ, 704, 548, doi: [10.1088/0004-637X/704/1/548](https://doi.org/10.1088/0004-637X/704/1/548)
- Pope, A., Scott, D., Dickinson, M., et al. 2006, MNRAS, 370, 1185, doi: [10.1111/j.1365-2966.2006.10575.x](https://doi.org/10.1111/j.1365-2966.2006.10575.x)
- Priddey, R. S., Gallagher, S. C., Isaak, K. G., et al. 2007, MNRAS, 374, 867, doi: [10.1111/j.1365-2966.2006.11200.x](https://doi.org/10.1111/j.1365-2966.2006.11200.x)
- Priddey, R. S., Ivison, R. J., & Isaak, K. G. 2008, MNRAS, 383, 289, doi: [10.1111/j.1365-2966.2007.12536.x](https://doi.org/10.1111/j.1365-2966.2007.12536.x)
- Reed, S. L., McMahan, R. G., Banerji, M., et al. 2015, MNRAS, 454, 3952, doi: [10.1093/mnras/stv2031](https://doi.org/10.1093/mnras/stv2031)

- Romano-Díaz, E., Choi, J.-H., Shlosman, I., & Trenti, M. 2011, *ApJ*, 738, L19, doi: [10.1088/2041-8205/738/2/L19](https://doi.org/10.1088/2041-8205/738/2/L19)
- Scott, S. E., Fox, M. J., Dunlop, J. S., et al. 2002, *MNRAS*, 331, 817, doi: [10.1046/j.1365-8711.2002.05193.x](https://doi.org/10.1046/j.1365-8711.2002.05193.x)
- Smail, I., Ivison, R. J., & Blain, A. W. 1997, *ApJ*, 490, L5, doi: [10.1086/311017](https://doi.org/10.1086/311017)
- Spergel, D. N., Bean, R., Doré, O., et al. 2007, *ApJS*, 170, 377, doi: [10.1086/513700](https://doi.org/10.1086/513700)
- Stevens, J. A., Page, M. J., Ivison, R. J., Smail, I., & Carrera, F. J. 2004, *ApJ*, 604, L17, doi: [10.1086/383314](https://doi.org/10.1086/383314)
- Stevens, J. A., Ivison, R. J., Dunlop, J. S., et al. 2003, *Nature*, 425, 264
- Stiavelli, M., Djorgovski, S. G., Pavlovsky, C., et al. 2005, *ApJ*, 622, L1, doi: [10.1086/429406](https://doi.org/10.1086/429406)
- Tamura, Y., Kohno, K., Nakanishi, K., et al. 2009, *Nature*, 459, 61, doi: [10.1038/nature07947](https://doi.org/10.1038/nature07947)
- Umehata, H., Tamura, Y., Kohno, K., et al. 2017, *ApJ*, 835, 98, doi: [10.3847/1538-4357/835/1/98](https://doi.org/10.3847/1538-4357/835/1/98)
- Venemans, B. P., McMahon, R. G., Warren, S. J., et al. 2007, *MNRAS*, 376, L76, doi: [10.1111/j.1745-3933.2007.00290.x](https://doi.org/10.1111/j.1745-3933.2007.00290.x)
- Venemans, B. P., Neeleman, M., Walter, F., et al. 2019, *ApJ*, 874, L30, doi: [10.3847/2041-8213/ab11cc](https://doi.org/10.3847/2041-8213/ab11cc)
- Venemans, B. P., Walter, F., Zschaechner, L., et al. 2015, *ApJ*, 816, 37, doi: [10.3847/0004-637X/816/1/37](https://doi.org/10.3847/0004-637X/816/1/37)
- Venemans, B. P., Findlay, J. R., Sutherland, W. J., et al. 2013, *ApJ*, 779, 24, doi: [10.1088/0004-637X/779/1/24](https://doi.org/10.1088/0004-637X/779/1/24)
- Wang, F., Yang, J., Fan, X., et al. 2019, *ApJ*, 884, 30, doi: [10.3847/1538-4357/ab2be5](https://doi.org/10.3847/1538-4357/ab2be5)
- Wang, R., Wagg, J., Carilli, C. L., et al. 2011, *AJ*, 142, 101, doi: [10.1088/0004-6256/142/4/101](https://doi.org/10.1088/0004-6256/142/4/101)
- Webb, T. M. A., Yee, H. K. C., Ivison, R. J., et al. 2005, *ApJ*, 631, 187, doi: [10.1086/432524](https://doi.org/10.1086/432524)
- Willott, C. J., Bergeron, J., & Omont, A. 2017, *ApJ*, 850, 108, doi: [10.3847/1538-4357/aa921b](https://doi.org/10.3847/1538-4357/aa921b)
- Willott, C. J., Percival, W. J., McLure, R. J., et al. 2005, *ApJ*, 626, 657, doi: [10.1086/430168](https://doi.org/10.1086/430168)
- Willott, C. J., Delorme, P., Omont, A., et al. 2007, *AJ*, 134, 2435, doi: [10.1086/522962](https://doi.org/10.1086/522962)
- Willott, C. J., Delorme, P., Reylé, C., et al. 2010, *ApJ*, 139, 906, doi: [10.1088/0004-6256/139/3/906](https://doi.org/10.1088/0004-6256/139/3/906)
- Yajima, H., Shlosman, I., Romano-Díaz, E., & Nagamine, K. 2015, *MNRAS*, 451, 418, doi: [10.1093/mnras/stv974](https://doi.org/10.1093/mnras/stv974)
- Yang, J., Wang, F., Fan, X., et al. 2019, *AJ*, 157, 236, doi: [10.3847/1538-3881/ab1be1](https://doi.org/10.3847/1538-3881/ab1be1)
- . 2021, *ApJ*, 923, 262, doi: [10.3847/1538-4357/ac2b32](https://doi.org/10.3847/1538-4357/ac2b32)
- Zhang, Y., Zheng, X. Z., Shi, D. D., et al. 2022, *MNRAS*, 512, 4893, doi: [10.1093/mnras/stac824](https://doi.org/10.1093/mnras/stac824)
- Zheng, W., Overzier, R. A., Bouwens, R. J., et al. 2006, *ApJ*, 640, 574, doi: [10.1086/500167](https://doi.org/10.1086/500167)